

Numerical modeling of thermal dust polarization from aligned grains in the envelope of evolved stars with updated POLARIS

Bao Truong,^{1,2}★ Thiem Hoang,^{1,2} Nguyen Chau Giang,^{1,2} Pham Ngoc Diep,³

Dieu D. Nguyen,⁴ Nguyen Bich Ngoc,^{3,5}

¹Korea Astronomy and Space Science Institute, 776 Daedeokdae-ro, Yuseong-gu, Daejeon 34055, Republic of Korea

²Department of Astronomy and Space Science, University of Science and Technology, 217 Gajeong-ro, Yuseong-gu, Daejeon 34113, Republic of Korea

³Department of Astrophysics, Vietnam National Space Center, Vietnam Academy of Science and Technology, 18 Hoang Quoc Viet, Hanoi, Vietnam

⁴Université de Lyon 1, Ens de Lyon, CNRS, Centre de Recherche Astrophysique de Lyon (CRAL) UMR5574, F-69230 Saint-Genis-Laval, France

⁵Graduate University of Science and Technology, Vietnam Academy of Science and Technology, 18 Hoang Quoc Viet, Hanoi, Vietnam

Accepted XXX. Received YYY; in original form ZZZ

ABSTRACT

Magnetic fields are thought to influence the formation and evolution of evolved star envelopes. Thermal dust polarization from magnetically aligned grains is potentially a powerful tool for probing magnetic fields and dust properties in these circumstellar environments. In this paper, we present numerical modeling of thermal dust polarization from the envelope of IK Tau using the magnetically enhanced radiative torque (MRAT) alignment theory implemented in our updated POLARIS code. Due to the strong stellar radiation field, the minimum size required for RAT alignment of silicate grains is $\sim 0.005 - 0.05 \mu\text{m}$. Additionally, ordinary paramagnetic grains can achieve perfect alignment by MRAT in the inner regions of $r < 500$ au due to stronger magnetic fields of $B \sim 10$ mG - 1G, producing thermal dust polarization degree of $\sim 10\%$. The polarization degree can be enhanced to $\sim 20 - 40\%$ for grains with embedded iron inclusions. We also find that the magnetic field geometry affects the alignment size and the resulting polarization degree due to the projection effect in the plane-of-sky. We also study the spectrum of polarized thermal dust emission and find the increased polarization degree toward $\lambda > 50 \mu\text{m}$ due to the alignment of small grains by MRAT. Furthermore, we investigate the impact of rotational disruption by RATs (RAT-D) and find the RAT-D effect cause a decrease in the dust polarization fraction. Finally, we compare our numerical results with available polarization data observed by SOFIA/HAWC+ for constraining dust properties, suggesting grains are unlikely to have embedded iron clusters and might have slightly elongated shapes. Our modeling results suggest further observational studies at far-infrared/sub-millimeter wavelengths to understand the properties of magnetic fields and dust in AGB envelopes.

Key words: Evolved stars – Circumstellar dust – Dust polarization

1 INTRODUCTION

The study of magnetic fields (B-fields) is essential for understanding various astrophysical processes in the Universe. In the late evolution of low- and intermediate-mass stars (i.e., $M_* \sim 0.5 - 8 M_\odot$, see Höfner & Olofsson 2018) as Asymptotic Giant Branch (AGB), magnetic fields likely play a crucial role in the mass-loss mechanism and the formation of a circumstellar envelope (Soker 2002; Thirumalai & Heyl 2013; Höfner & Olofsson 2018). Theoretical models showed that the oscillating Alfvén waves by stellar magnetic fields could efficiently levitate stellar materials above the atmosphere and, later on, stellar winds are produced by radiation pressure on the newly formed grains (Airapetian et al. 2000; Airapetian et al. 2010; Cranmer & Saar 2011; Höfner & Olofsson 2018). Additionally, magnetic fields in a close binary system during post-AGB phases could shape the dusty winds from a spherical structure to a bipolar structure before being exploded as planetary nebulae (PNe) (e.g., García-Segura et al. 1999; Vlemmings et al. 2006; Nordhaus et al. 2007), significantly

contributing to explaining the “breaking asymmetry” as shown in pre-PNe/PNe observations (Sabin et al. 2007; Sabin et al. 2015).

Magnetic fields in AGB/post-AGB envelopes have been mostly studied through polarimetric observations of maser lines by the Zeeman effect. The polarized maser emission from molecules such as SiO, H₂O, and OH were observed in the specific regions of AGB envelopes (Boboltz & Diamond 2005; Leal-Ferreira et al. 2013) and PNe (Vlemmings et al. 2006). The profiles of polarized maser lines could be used to measure the magnetic field strength and constrain the configuration of magnetic fields in circumstellar envelopes (see in Vlemmings 2019). However, the maser lines strongly depend on the radiative or collisional pumping in the local very dense clumps in the envelopes, which may resolve a small portion of AGB outflows and only reveal small-scale components of the magnetic fields (Soker 2002; Vlemmings 2019). Also, the stellar magnetic fields could be measured via non-maser molecular line emission by the Goldreich-Kylafis effect (Vlemmings et al. 2012; Huang et al. 2020); however, there are uncertainties in polarization direction which could either parallel or perpendicular to the magnetic field lines (Kylafis 1983). Therefore, it is important to measure magnetic fields on a global

★ Email: baotruong@kasi.re.kr

scale in order to examine their contribution to driving winds in the evolved star's envelopes.

Polarized thermal dust emission from magnetically aligned grains is a powerful tool for mapping magnetic fields in a large-scale circumstellar envelope of evolved stars (see a review of Scicluna et al. 2020). Following the idea of the magnetic alignment of spinning grains with their longest axes perpendicular to the local magnetic fields, the magnetic field can be mapped from thermal dust polarization (see Hildebrand 1988). The study of thermal dust polarization in post-AGB and PNe objects has been presented in sub-millimeter (sub-mm) observations by the James Clerk Maxwell Telescope (JCMT), Combined Array for Research in Millimeter-wave Astronomy (CARMA), and Atacama Large Millimeter Array (ALMA) such as NGC 7027, NGC 6537, NGC 6302 (e.g., Greaves 2002; Sabin et al. 2007) and OH 231.8+4.2 (e.g., Sabin et al. 2015; Sabin et al. 2020), revealing different magnetic field geometries and probing their major roles in shaping these nebulae. Vlemmings et al. (2017) first observed thermal dust polarization by aligned grains within the envelope of evolved stars as VY CMa by ALMA at 178 GHz. Andersson et al. (2022) observed the polarized thermal emission from carbonaceous grains at far-infrared (far-IR) wavelengths in the envelope of IRC+10216 by Stratospheric Observatory for Infrared Astronomy (SOFIA)/High-resolution Airborne Wideband Camera-plus (HAWC+).

Furthermore, thermal dust polarization is vital for exploring dust properties in AGB/post-AGB envelopes. Thermal dust polarization at far-IR/sub-mm wavelengths opens the possibility to trace large grains of $a > 0.1 \mu\text{m}$ (e.g., Vlemmings et al. 2017; Andersson et al. 2022), while optical/near-IR polarization by scattered light could characterize the existence of smaller grains of $a < 0.1 \mu\text{m}$ (e.g., Khouri et al. 2016; Adam & Ohnaka 2019). In addition, the features of dust polarization provide a more detailed picture of the physical properties of circumstellar dust in AGB envelopes, e.g., grain shape, size distribution, chemical compositions, and their porosity (see Hensley & Draine 2021), which extends our knowledge of dust enrichment in the interstellar medium (ISM) through stellar ejecta (see the review of Tielens et al. 2005 and De Beck et al. 2019).

Nevertheless, the potential of dust polarization from aligned grains in probing magnetic fields and dust properties in evolved star envelopes is still unclear due to the lack of a detailed study of grain alignment and resulting dust polarization in this environment. The alignment process of dust grains, in general, includes two main stages: (1) the alignment of the grain axis of maximum moment of inertia, \mathbf{a}_1 , with the grain angular momentum, \mathbf{J} , (so-called internal alignment), and (2) the alignment of the angular momentum \mathbf{J} with a preferred direction in space such as radiation fields \mathbf{k} or magnetic fields \mathbf{B} (so-called external alignment). The former process has been studied extensively for interstellar grains (Purcell 1979) and grains in protostellar environments (Hoang et al. 2022). For the latter, it is recently established that the leading theory of grain alignment is based on RAdiative Torques (hereafter RATs, see Dolginov & Mitrofanov 1976; Draine & Weingartner 1996; Lazarian & Hoang 2007). The RAT theory has been developed with quantitative predictions for various environmental conditions (Hoang & Lazarian 2014) and dust compositions (Hoang & Lazarian 2016) and successfully tested with observations of local environments as diffuse ISM and molecular clouds (MCs) (see reviews of Andersson et al. 2015; Tram & Hoang 2022). The RAT theory has also been extended with the combined effects of RATs and magnetic relaxation (i.e., Magnetically Enhanced RAdiative Torque or MRAT, see Hoang & Lazarian 2016 and Hoang et al. 2022). The MRAT theory demonstrates the key role of embedded irons inside grains in enhancing the RAT alignment efficiency.

In addition, for an environment close to an intense radiation source such as AGB envelopes and PNe, the dust properties can be modified by a mechanism called RAdiative Torque Disruption (hereafter RAT-D), first introduced by Hoang et al. (2019). The basic idea is that the induced RATs from strong radiation fields effectively spin up large grains to suprathermal rotation and, later on, disrupt them into smaller fragments by centrifugal stress. As a result, the RAT-D mechanism removes a large amount of large grains in local environments, constraining the maximum size at which grains can survive by RAT-D and modifying the original grain size distribution. The effects of RAT-D mechanism on the physical properties of surrounding dust grains were numerically examined in many astrophysical environments such as cosmic transients (Hoang et al. 2020; Giang & Hoang 2021; Giang et al. 2022), radiative pressure from massive protostars (Hoang et al. 2021), and in the evolved star envelopes (Tram et al. 2020; Truong et al. 2022). Numerical modeling by Lee et al. (2020) showed the rotational disruption by RATs reduces the degree of thermal dust polarization due to the removal of large grains near intense radiation sources. The evidence of RAT-D was found in polarimetric observations in star-forming MCs (e.g., Ngoc et al. 2021; Tram et al. 2021a; Tram et al. 2021b; Hoang T. D. et al. 2022).

Understanding thermal dust polarization from aligned grains in evolved star envelopes requires synthetic modeling based on the basic physics of grain alignment and disruption induced by RATs. Recently, Reissl et al. (2016) developed the POLARized RadIation Simulator (POLARIS) - a three-dimensional simulation code describing multi-wavelength polarization in local environments through the combination of the improved RAT theories and the radiative transfer of dust emission and polarization. The code was successfully used to model the RAT alignment and reproduce the observed polarization in MCs (Seifried et al. 2019; Seifried et al. 2020; Reissl et al. 2021) and diffuse ISM (Reissl et al. 2020), in which the gas density is lower with $n_{\text{gas}} \sim 10^2 - 10^6 \text{cm}^{-3}$. However, in very dense regions such as protostellar environments and evolved star envelopes with $n_{\text{gas}} > 10^6 \text{cm}^{-3}$, the physics of grain alignment is quite complicated due to stronger gas randomization. Hoang (2022) and Hoang et al. (2022) conducted a detailed theoretical study for grain alignment in protostellar environments using the RAT paradigm. The authors concluded that the high dust polarization level of up to 20 – 40% observed in protostellar environments by ALMA (Hull et al. 2014; Cox et al. 2018) could only be reproduced by the MRAT mechanism for grains having iron inclusions (Hoang & Lazarian 2016). Giang et al. (2023) implemented the MRAT mechanism into POLARIS and successfully applied it for modeling synthetic dust polarization in protostellar cores and disks. The updated POLARIS is potentially applied in circumstellar envelopes of evolved stars, in which strong stellar magnetic fields of $\sim \text{mG-G}$ (Vlemmings et al. 2017; Vlemmings 2019) could produce efficient internal and external alignment by MRAT (Hoang & Lazarian 2016) and then be expected to produce a high degree of thermal dust polarization. The updated code is currently being upgraded (Giang et al., in preparation) by incorporating the RAT-D for modeling dust polarization from regions of intense radiation fields, such as massive protostellar environments, photodissociation regions, and cosmic transients.

This paper first studies dust polarization from aligned grains in AGB envelopes based on our current understanding of RAT theories through synthetic dust polarization modeling using the updated POLARIS. We investigate the basic properties of both internal and external alignment and rotational disruption by RATs in the circumstellar envelope (CSE) of O-rich AGB stars, particularly IK Tauri (a.k.a IK Tau or NML Tauri). It is a Mira variable star pulsating in a period of ~ 470 days (Wing & Lockwood 1973; Hale et al. 1997), in the late

evolutionary phase of a low-mass star of $M_* \sim 1.5 M_\odot$ (Gobrecht et al. 2016). Observations at optical and sub-millimeter wavelengths showed the IK Tau CSE with a roughly spherical structure (Marvel 2005; Kim et al. 2010; Adam & Ohnaka 2019). Composed of O-rich dust as alumina, pyroxene, crystalline olivine, and amorphous silicate (Gobrecht et al. 2016; Decin et al. 2018), circumstellar grains in the IK Tau envelope are expected to achieve efficient magnetic alignment by MRAT due to a strong stellar magnetic field (Boboltz & Diamond 2005; Leal-Ferreira et al. 2013). We then model the polarized dust emission from spinning circumstellar grains in the IK Tau CSE by utilizing the power of POLARIS in numerically solving polarized radiative transfer. The modeling results will be compared with the available observation by SOFIA/HAWC+ (Andersson et al. in preparation) at far-IR/sub-mm wavelengths to constrain the underlying properties of dust and magnetic fields in the IK Tau envelope.

The rest of this paper is structured as follows. Section 2 describes the model set-up based on the environmental conditions of the IK Tau envelope and the magnetic field morphology. We will subsequently describe the processes of performing synthetic continuum dust polarization modeling in POLARIS following the fundamental physics of grain alignment and disruption by RATs in Section 3. The numerical results of grain alignment and disruption, as well as the modeling results of dust polarization, are presented in Section 4. We will discuss the implications of our results for interpreting observations along with the applications in studying magnetic fields and constraining dust properties in evolved star envelopes in Section 5. Our main findings are finally summarized in Section 6.

2 INITIAL CONDITIONS OF AN AGB ENVELOPE

2.1 Circumstellar envelope gas structure

We focus on modeling thermal dust polarization from aligned grains in a specific circumstellar envelope of IK Tau. For the gas properties, we consider the gas profile expanding spherically at a constant velocity by dust-driven winds (see Höfner 2008; Höfner et al. 2016; Tram et al. 2020). The density of hydrogen gas (i.e., $m_{\text{gas}} = m_{\text{H}} = 1$ amu) in the envelope at a distance r from the central star is calculated as

$$n_{\text{gas}}(r) = \frac{\dot{M}}{4\pi r^2 m_{\text{gas}} v_{\text{exp}}} \approx 4.5 \times 10^5 \left(\frac{\dot{M}}{10^{-5} M_\odot \text{ yr}^{-1}} \right) \left(\frac{10 \text{ km s}^{-1}}{v_{\text{exp}}} \right) \times \left(\frac{100 \text{ au}}{r} \right)^2 \text{ cm}^{-3}, \quad (1)$$

where \dot{M} is the mass-loss rate and v_{exp} is the expansion velocity; adopting $\dot{M} = 4.5 \times 10^6 M_\odot \text{ yr}^{-1}$ and $v_{\text{exp}} = 24 \text{ km s}^{-1}$ in the conditions of IK Tau envelope (see Table 1). The gas density decreases significantly with $\sim r^{-2}$ from $n_{\text{gas}} \sim 10^8 \text{ cm}^{-3}$ at $r = 18 \text{ au}$ to $n_{\text{gas}} \sim 10^2 \text{ cm}^{-3}$ at $r \sim 10000 \text{ au}$. The profile of gas density is plotted by a dashed green line in the lower panel of Figure 1.

For numerical calculations, we construct the model of the IK Tau CSE with a symmetric structure (Decin et al. 2010; Adam & Ohnaka 2019) on a three-dimensional spherical grid of $N_r \times N_\theta \times N_\phi = 151 \times 61 \times 61$, where N_r , N_θ and N_ϕ are the number of grid cells in radial, polar and azimuth directions. The inner boundary is set at 18 au, where circumstellar dust is first condensed and formed within the IK Tau CSE. The outer boundary is set at 40000 au, where circumstellar winds interact with the ISM (see in Decin et al. 2010;

Table 1. Modeling parameters used in POLARIS

Parameters	Values	References
Circumstellar envelope model		
Inner boundary (R_{in})	18 au	(1)
Outer boundary (R_{out})	40,000 au	(1)
Mass-loss rate (\dot{M})	$4.5 \times 10^{-6} M_\odot \text{ yr}^{-1}$	(1)
Expansion velocity (v_{exp})	24 km s^{-1}	(1); (2)
Stellar radiation source		
Stellar luminosity (L_*)	$8724 L_\odot$	(3)
Stellar radius (R_*)	$608 R_\odot$	(3)
Stellar mass (M_*)	$1.5 M_\odot$	(1); (4)
Effective temperature (T_*)	2234 K	(3)
Distance to observer (d_*)	265 pc	(1); (5)
Dust model		
Chemical composition	silicate	(6); (9)
Minimum grain size (a_{min})	5 nm	-
Maximum grain size (a_{max})	$0.5 \mu\text{m}$	(7)
Size distribution	$C a^{-3.5}$	-
Dust-to-gas mass ratio ($M_{\text{d/g}}$)	0.005	(6)
Grain axial ratio (s)	0.5	-
Iron fraction (f_{p})	0.01 - 0.1	(8)
Volume filling factor (ϕ_{sp})	0.005	(8)
Level of iron clusters (N_{cl})	$10 - 10^3$	(8)

References: (1) Decin et al. (2010); (2) Maercker et al. (2016); (3) Adam & Ohnaka (2019); (4) Fox & Wood (1985); (5) Hale et al. (1997); (6) Gobrecht et al. (2016); (7) Scicluna et al. (2015); (8) Hoang & Lazarian (2016); (9) Decin et al. (2018)

Tram et al. 2020). The characteristics of the IK Tau CSE are described in Table 1.

2.2 Magnetic field morphology

The maser measurements of molecular lines (e.g., SiO, H₂O, OH) reveal the variation of the magnetic field strength with the radial distance from inner to outer regions within the envelope. The radial profile of the circumstellar magnetic field strength indicates different scenarios of magnetic field geometry, as $B \propto r^{-2}$ for solar-like structure and $B \propto r^{-1}$ for toroidal structure (see Vlemmings 2019).

We adopt the model of a solar-like magnetic field with a dipole configuration, following the interpretation of magnetic field geometry in IK Tau envelope by Leal-Ferreira et al. (2013), which is presented in the upper panels of Figure 1. The white segments present the pattern of stellar magnetic field lines in the xy -plane (upper left panel) and the xz -plane (upper right panel). The stellar magnetic fields generally reveal the azimuthal pattern when observed in the xy -plane. Meanwhile, as observed in an edge-on view (i.e., xz -plane), the magnetic fields show the morphology of a dipole structure along the z -direction.

The dependence of stellar magnetic field strength on the envelope distance is assumed to follow $B \propto r^{-2.1}$, based on the results derived from SiO, and H₂O maser polarization by Boboltz & Diamond (2005) and Leal-Ferreira et al. (2013), as plotted by a dashed black line in the lower panel of Figure 1. The B-field strength is considerably high at 1 - 3 G in the inner region of $r \sim 18 \text{ au}$ near the central star. Moving to the outer region of $r \sim 10000 \text{ au}$, the B-field strength decreases to $\sim 10 \mu\text{G}$ - close to the standard magnetic field strength of the diffuse ISM (Crutcher 2012).

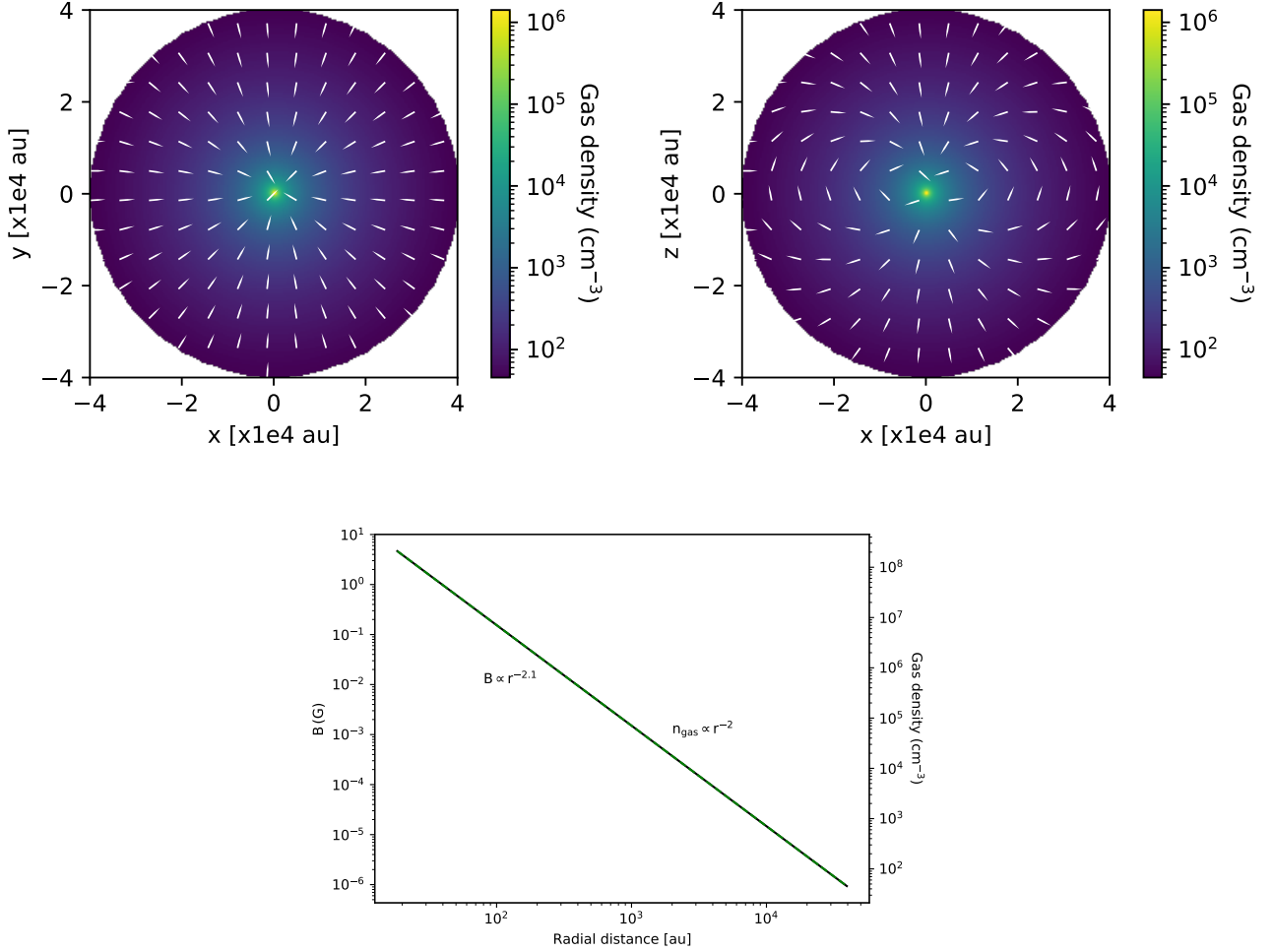


Figure 1. Dipole structure of IK Tau’s magnetic field observed in the xy -plane (upper left panel) and the xz -plane (upper right panel). The lower panel illustrates the strength of the stellar magnetic field with $B \propto r^{-2.1}$ (solid black line) and the gas density profile in the IK Tau circumstellar envelope (dashed green line).

3 MODELING OF GRAIN ALIGNMENT AND DUST POLARIZATION WITH UPDATED POLARIS

Considering the profiles of gas density and stellar magnetic fields as modeling inputs, we perform synthetic dust continuum polarization calculation by the updated POLARIS code (Reissl et al. 2016; Giang et al. 2023). In this section, we briefly describe the simulation processes in POLARIS, including (1) the radiative transfer calculation of dust heating by the Monte Carlo technique, (2) the measurement of aligned grains based on RAT alignment theories, (3) and the polarized radiative transfer calculation for modeling thermal polarized emission from aligned grains in AGB envelopes.

3.1 Dust heating radiative transfer calculation

Firstly, we investigate the dust heating and cooling processes in AGB envelopes by numerically solving radiative transfer by POLARIS. For the main radiation source, we consider circumstellar grains receive photons mostly from the central AGB star. The central stellar radiation of IK Tau can be described as a blackbody with the effective temperature of 2234 K and the bolometric luminosity of $L_* = 8724 L_\odot$ (Adam & Ohnaka 2019, see Table 1). We assume the spectral energy distribution (SED) of IK Tau spanning from $\lambda_{\min} = 0.1 \mu\text{m}$ - the lower limit at which all photons are absorbed by the photoionization

of hydrogen atoms, to $\lambda_{\max} = 3 \text{ mm}$ - the upper limit at which RAT efficiency is negligible. Note that besides the impact of stellar radiation, circumstellar dust can be affected by interstellar radiation fields (ISRF) from the outer boundary of the IK Tau envelope, which is negligible and is not considered in our calculation.

For the dust model, we consider the composition of O-rich materials with 100% of silicate grains presented in the IK Tau envelope, assuming the oblate shape with the ratio of the semi-minor and semi-major axes of grains $s = 1/2$ and the size varying in the range from $a_{\min} = 5 \text{ nm}$ to $a_{\max} = 0.5 \mu\text{m}$ (Scicluna et al. 2015; Truong et al. 2022). The grain size distribution (GSD) is followed by the standard Mathis-Rumpl-Nordsieck (MRN) size distribution (Mathis et al. 1977) as $dn \propto Ca^{-3.5} da$, where a is the effective size of grains and C is the normalization constant derived from the total dust-to-gas mass ratio $M_{\text{d/g}}$ (Giang et al. 2023). Our works assume the dust-to-mass ratio of 0.005 in the entire envelope of IK Tau (Gobrecht et al. 2016), which is lower than the standard $M_{\text{d/g}} = 0.01$ in the diffuse ISM (Cardelli et al. 1989). Details about the radiation source and the dust model in the IK Tau CSE are presented in Table 1.

Given the radial distribution of gas density (see Section 2.1) and the dust profile, POLARIS could model the propagation of light from the main source in the dusty environment as AGB envelopes. In each grid cell of the model space, the code simulates the interaction

between incident photons and circumstellar dust using the Monte Carlo technique (Lucy 1999). Consequently, the code spontaneously updates the grain temperature T_d , followed by the balance of radiation absorption and thermal dust emission (Lucy 1999; Reissl et al. 2016; Giang et al. 2023). POLARIS stores the radiation energy density u_λ and the mean propagation directions of photons from the processes of radiation absorption, dust emission, and dust scattering in each grid cell, giving the anisotropic degree of radiation γ_λ (Bethell et al. 2007; Reissl et al. 2016) required to model RAT alignment in the following step.

3.2 Modeling grain alignment and disruption driven by RATs

3.2.1 Magnetic properties of grains

Iron locked inside dust grains is taken into consideration in the studies of magnetic alignment, which is expected to be presented during the formation and evolution of silicate grains in O-rich AGB envelopes (Jones 1990; Höfner et al. 2022). Iron atoms can be diffusely distributed within dust grains, making them paramagnetic (PM) material. Iron can also be embedded and formed in cluster distribution (Jones & Spitzer 1967), in which each iron cluster can be considered as a large magnetic moment, and grains become superparamagnetic (SPM). Hoang & Lazarian (2016) showed the presence of iron plays an essential role in the interaction of dust and the ambient magnetic fields, described by the magnetic susceptibility for different magnetic materials (see the review in Hoang et al. 2022). Generally, SPM grains show higher magnetic susceptibility than PM grains, and the magnetic susceptibility increases with increasing levels of iron inclusion N_{cl} , varying from 20 to 10^5 (Jones & Spitzer 1967).

In the updated version of POLARIS by Giang et al. (2023), the calculation of PM and SPM grains' magnetic susceptibility was included in the grain alignment modeling. Here, we apply in circumstellar grains in the IK Tau envelope, considering the model of PM materials with $f_p = 0.01$ and $f_p = 0.1$, corresponding to the configurations of 1% and 10% of Fe atoms randomly distributed inside grains, respectively. For SPM grains, we consider the increasing level of iron inclusions $N_{cl} = 10 - 10^3$ with a fixed volume filling factor of Fe atoms in each cluster $\phi_{sp} = 0.005$ (Hoang & Lazarian 2016), corresponding to 1.67% of Fe abundance presented as a form of clusters in grain. The magnetic properties of PM and SPM grains are presented in Table 1.

3.2.2 Internal alignment by Barnett relaxation

When circumstellar grains rotate at a certain angular speed Ω , all electron spins inside grains will be reoriented along Ω and induce the magnetic moment by the Barnett effect (see Barnett 1915). Theoretical studies of Purcell (1979) showed that the induced magnetic moment for a magnetic rotating grain could dissipate the grain rotational energy to the minimum energy level at which grains can stably rotate around the minor axis of grain moment inertia \mathbf{a}_1 (i.e., internal alignment with $\mathbf{J} \parallel \Omega \parallel \mathbf{a}_1$, see the illustration in Hoang et al. (2022) and references therein). This phenomenon is called the internal alignment by the Barnett relaxation, and grains can certainly achieve this state if Barnett magnetic relaxation has a shorter timescale than the randomization by gas collisions (i.e., $\tau_{BR} < \tau_{gas}$). Otherwise, grains will have slow internal relaxation, at which grains may rotate around their major or minor axes of inertia moment (see Hoang & Lazarian 2016 and Hoang et al. 2022). In general, large grains tend to have slow internal relaxation because of their large inertia moment, but this issue can be solved if grains have a higher rotational speed or

high levels of iron inclusions (e.g., Hoang & Lazarian 2016; Hoang et al. 2022; Giang et al. 2023).

The internal alignment characteristics of magnetic grains were considered in the updated version of POLARIS by Giang et al. (2023). The code first computed the critical sizes having fast internal relaxation [$a_{min,aJ} - a_{max,aJ}$], following the condition of $\tau_{BR} = \tau_{gas}$, then determined the internal alignment degree for polarized RT modeling in the third simulation (see Giang et al. 2023). The states of internal alignment depend on the rotational properties of grains and will be described in the following sections.

3.2.3 External alignment with Magnetic fields

As being magnetized by the Barnett effect, the induced magnetic moment will interact with the ambient magnetic field \mathbf{B} , producing a magnetic torque that causes the precession of the angular momentum \mathbf{J} around \mathbf{B} (i.e., Larmor precession, see the illustration in Hoang et al. 2022). Grains are considered to be stably rotated around \mathbf{B} -fields if the Larmor precession happens faster than the gas randomization (i.e., $\tau_{Lar} < \tau_{gas}$), at which the magnetic field is considered as the preferred axis of alignment (so-called magnetic alignment, see Hoang & Lazarian 2016; Hoang et al. 2022).

The external magnetic alignment can happen due to the dissipation of rotational energy caused by the misalignment between \mathbf{J} and \mathbf{B} (so-called David-Greenstein mechanism of magnetic relaxation, see in Davis & Greenstein 1951). The efficiency of magnetic relaxation is characterized by the magnetic relaxation parameter $\delta_m = \tau_{gas}/\tau_{mag}$, which was included in the updated POLARIS (Giang et al. 2023). The code could calculate the maximum size $a_{max,JB}^{DG}$ at which magnetic relaxation is faster than gas randomization (i.e., $\delta_m > 1$). Generally, large grains could have faster magnetic relaxation than small grains, and SPM grains achieve more effective magnetic relaxation than PM grains because of higher magnetic susceptibility (Hoang & Lazarian 2016; Hoang et al. 2022). However, Hoang & Lazarian (2016) showed that even for SPM grains with $\delta_m \gg 1$, magnetic relaxation itself provides the external alignment but with a low alignment degree in the absence of grain suprathreshold rotation.

3.2.4 Radiative Torque Alignment (RAT-A) Paradigm

The interaction of stellar radiation with a helical grain can induce RATs due to the difference in scattering/absorption between left- and right-handed circularly polarized photons (Dolginov & Mitrofanov 1976; Lazarian & Hoang 2007). Here we recall the paradigm of magnetic alignment induced by RATs, which is essential for interpreting grain alignment in AGB circumstellar environments.

The RATs induced by strong radiation from the central source can spin up circumstellar grains and achieve the maximum angular velocity $\Omega \sim \Omega_{RAT}$, which is given by

$$\Omega_{RAT} = \frac{\Gamma_{RAT} \cos \psi \tau_{damp}}{I_{\parallel}}, \quad (2)$$

where $I_{\parallel} = 8\pi\rho a^5/15$ is the moment of inertia in the minor axis of grains \mathbf{a}_1 and ψ is the angle between the directions of the magnetic field \mathbf{B} and radiation field \mathbf{k} (Giang et al. 2023). Γ_{RAT} is the radiative torque acting on the grain size a by stellar radiation, which is defined as

$$\Gamma_{RAT} = \int_{\lambda_{min}}^{\lambda_{max}} \pi a^2 \gamma_\lambda u_\lambda \left(\frac{\lambda}{2\pi} \right) Q_\Gamma d\lambda, \quad (3)$$

where Q_Γ is the RAT efficiency depending on the grain size a and the

wavelength of incident photons λ (see the numerical calculation in [Lazarian & Hoang 2007](#)). u_λ and γ_λ are the spectral energy density and the average anisotropic degree derived from the first simulation in Section 3.1, respectively.

Nevertheless, the combined effects of gas randomization and grain cooling by IR emission can slow down the rotation of grains by RATs. The term $\tau_{\text{damp}} = \tau_{\text{gas}}/(1 + F_{\text{IR}})$ in Equation 2 describes the characteristic rotational damping timescale, where τ_{gas} is the damping by gas collisions and F_{IR} is the dimensionless damping coefficient due to IR re-emission (see the derivation in [Hoang et al. 2022](#)).

Besides the spin-up effect, the RATs by stellar radiation can cause the alignment between the angular momentum \mathbf{J} and \mathbf{B} by the alignment torque components ([Lazarian & Hoang 2007](#); [Hoang & Lazarian 2008](#); [Hoang & Lazarian 2016](#)). The studies of [Hoang & Lazarian \(2008\)](#) showed that a fraction $f_{\text{high-J}}$ of grains can achieve suprathermal rotation by RATs (i.e., high-J attractors with $\Omega > \Omega_{\text{ther}}$). Then, they could achieve efficient internal and external alignment and be stably aligned parallel to B-fields (see in [Hoang et al. 2022](#)). Meanwhile, the remaining portion $1 - f_{\text{high-J}}$ of grains rotate subthermally by gas collisions (i.e., low-J attractors with $\Omega \sim \Omega_{\text{ther}}$). Consequently, they have inefficient internal alignment due to thermal fluctuation of electron spins inside grains ([Purcell 1979](#)) and inefficient external alignment with B-fields. The value of $f_{\text{high-J}}$ can range from 0.2 to 0.7 for irregular grains ([Herranen et al. 2021](#)).

Theoretical and numerical studies of [Hoang & Lazarian \(2016\)](#) illustrated the combined effect of magnetic relaxation and grain alignment induced by RATs could increase the RAT alignment efficiency and leads to the perfect external alignment with \mathbf{B} (i.e., MRAT mechanism, see also in [Hoang et al. 2022](#)). This mechanism is more effective for PM grains located in strong magnetic field environments or SPM grains with iron inclusions due to enhanced magnetic relaxation, resulting in the high abundance of grains at high-J attractors with $f_{\text{high-J}} = 1$.

[Giang et al. \(2023\)](#) first considered the enhanced RAT alignment by magnetic relaxation in the updated POLARIS. The code considered the dependence of $f_{\text{high-J}}$ on the magnetic relaxation parameter (see Equation 28 in [Giang et al. 2023](#)), and thus, determined the maximum grain sizes having $f_{\text{high-J}} = 0.5$ (i.e., $a_{\text{max,JB}}^{\text{DG-0.5}}$) and $f_{\text{high-J}} = 1$ (i.e., $a_{\text{max,JB}}^{\text{DG-1}}$). Then, the code took into account the nature of grains at high-J and low-J attractors in the calculation of aligned grain sizes and the alignment degree (see the flow chart in [Giang et al. 2023](#)). In terms of internal alignment, within the critical sizes $[a_{\text{min,aJ}}^{\text{high-J}} - a_{\text{max,aJ}}^{\text{high-J}}]$ for grains at high-J attractors and $[a_{\text{min,aJ}}^{\text{low-J}} - a_{\text{max,aJ}}^{\text{low-J}}]$ for grains at low-J attractors, we set the alignment degree with $Q_{\text{X,high-J}} = 0.15$ and $Q_{\text{X,low-J}} = 0.05$, respectively. In terms of external alignment, the code calculated the minimum size of aligned grains, a_{align} , determined by the suprathermal condition induced by RATs, $\Omega_{\text{RAT}} \geq 3\Omega_{\text{ther}}$ ([Hoang & Lazarian 2008](#)). The maximum alignment size is determined by the Larmor precession, $a_{\text{max,JB}}^{\text{Lar}}$, is given by $\tau_{\text{Lar}} \leq \tau_{\text{gas}}/10$. Within the critical size of $[a_{\text{align}} - a_{\text{max,JB}}^{\text{Lar}}]$, PM and SPM grains aligned at high-J and low-J attractors have perfect external alignment, with the alignment degree $Q_{\text{J,high-J}} = Q_{\text{J,low-J}} = 1$.

3.2.5 Rotational disruption by RATs (RAT-D)

While being spun up at suprathermal rotation, circumstellar grains experience centrifugal stress pointing outward from the center of the grain mass. If grains reach the critical velocity at which the centrifugal stress exceeds the binding energy of grains, they start to

be disrupted by RATs (i.e., Radiative Torque Disruption (RAT-D) mechanism, see [Hoang et al. 2019](#); [Hoang et al. 2021](#)). The critical velocity Ω_{disr} at which RAT-D happens is therefore calculated as

$$\Omega_{\text{disr}} = \frac{2}{a} \left(\frac{S_{\text{max}}}{\rho} \right)^{1/2} \approx 3.6 \times 10^9 a_{-5}^{-1} \hat{\rho}^{-1/2} S_{\text{max,9}}^{1/2} \text{ rad s}^{-1}, \quad (4)$$

where $\hat{\rho} = \rho/3.3$ is the grain mass density, and $S_{\text{max,9}} = S_{\text{max}}/(10^9 \text{ erg cm}^{-3})$ is the maximum tensile strength of grains. The values of S_{max} characterizes the grain internal structure, with $S_{\text{max}} < 10^9 \text{ erg cm}^{-3}$ for porous/composite grains and $S_{\text{max}} \geq 10^9 \text{ erg cm}^{-3}$ for compact/crystalline grains (see [Hoang et al. 2019](#)).

As discussed in [Hoang et al. \(2019\)](#), the RAT-D disrupts large grains into smaller species, modifying the original grain size distribution $dn \propto Ca^\eta da$ with $\eta < -3.5$, implying the enhancement of small grains (see [Giang et al. 2020](#); [Giang & Hoang 2021](#); [Giang et al. 2022](#)). The mechanism is more effective as grains are exposed to strong radiation from evolved stars and considered in interpreting stellar observations ([Tram et al. 2020](#); [Truong et al. 2022](#)). We include the RAT-D effect in the main modeling by considering the calculation of maximum grain size after disruption a_{disr} and the grain size distribution with the modified slope η , which is currently developed in the newest version of POLARIS ([Giang et al., in preparation](#)).¹

3.3 Polarized radiative transfer calculation

Lastly, synthetic dust polarization in AGB envelopes is calculated by solving the radiative transfer equations of polarized radiation described by the Stokes parameters $[I, Q, U, V]^T$, where I presents the radiation intensity, Q and U present the linear polarization, and V presents the circular polarization. The polarized radiative transfer equations take into account the extinction, emission, and polarization properties observed in the plane-of-sky (see [Martin 1974](#); [Reissl et al. 2016](#)), as well as the degree of both internal and external alignment ([Greenberg 1968](#); [Reissl et al. 2016](#)). Given the information of radiation from the first simulation (Section 3.1), grain properties from grain alignment modeling (Section 3.2) and the conditions of the IK Tau envelope as gas density and magnetic field morphology (Section 2), POLARIS ([Reissl et al. 2016](#)) applies the ray-tracing technique to trace the light propagation through grid cells to the observer and uses the Runge-Kutta Fehlberg (RFK45) method to solve the full radiative transfer of Stokes parameters. The final results are the modeled degree of linear polarization p (%) described as

$$p(\%) = 100 \frac{\sqrt{Q^2 + U^2}}{I}, \quad (5)$$

and the polarization angle (PA)

$$PA = \frac{1}{2} \arctan \left(\frac{Q}{U} \right). \quad (6)$$

The updated version of POLARIS by [Giang et al. \(2023\)](#) improved the polarized radiative transfer calculations by incorporating the modern physics of grain alignment, which is based on the combined effect of RATs and magnetic relaxation ([Hoang & Lazarian 2016](#); [Hoang et al. 2022](#)). The effects of internal alignment for grains at high-J and low-J were considered in calculating the Rayleigh reduction factor R (see Section 4.2.5 in [Giang et al. 2023](#)). The roles

¹ In [Lazarian & Hoang \(2021\)](#), the effect of the RAT-D mechanism depends on the rotational properties of grains at high-J or low-J attractors. For the sake of simplicity, we consider the disruption occurring for all grains $a > a_{\text{align}}$ having magnetic alignment by RATs.

of embedded iron in enhancing RAT alignment were also considered in updating dust polarization calculation, allowing us to examine the MRAT effects for different magnetic properties of grains on dust polarization in AGB envelopes.

4 NUMERICAL RESULTS

4.1 Radiation and dust temperature distribution

Figure 2 illustrates the numerical results of stellar radiation distribution as a function of the envelope distance as a result of the interaction between circumstellar dust and stellar photon, including radiation strength U_{rad} (top panel), the average anisotropy degree γ_{rad} (middle panel) and the average dust temperature T_{d} (bottom panel). Generally, circumstellar dust is heated by the luminous stellar radiation in the innermost envelope of 18 au to the temperature of ~ 700 K - below the threshold temperature of silicate grain sublimation of ~ 1500 K (see [Draine & Salpeter 1979](#); [Draine & Lee 1984](#); [Draine 2011](#)). The radiation becomes less anisotropic (i.e., $\gamma_{\text{rad}} \sim 0.4$) due to the strong scattering between circumstellar dust and incident photons from the central star as well as thermal emission of hot dust in the very dense envelope. At a larger distance of $r > 18$ au, both stellar radiation U_{rad} and dust temperature T_{d} decrease with increasing the envelope distance and achieve $T_{\text{d}} < 100$ K in the outer region of the IK Tau CSE. And the value of γ_{rad} increases up to ~ 1 , resulting from the weak interaction between thermal dust emission and circumstellar dust in the outer envelope.

4.2 Grain alignment and disruption size distribution

From the modeled stellar radiation and dust temperature, we then investigate their effects on grain alignment and disruption induced by RATs. In this section, we present our modeling results of RAT alignment and rotational disruption paradigm in the IK Tau envelope, with the incorporated impacts of magnetic properties of dust grains from PM to SPM grains with iron inclusions.

4.2.1 Critical sizes for external grain alignment by RATs a_{align} ,

$$a_{\text{max,JB}}^{\text{Lar}}$$

Figure 3 shows the calculation of the minimum and maximum sizes having external alignment driven by RATs, denoted by a_{align} and $a_{\text{max,JB}}^{\text{Lar}}$. We consider the major effects of magnetic properties for both PM and SPM grains with increasing level of iron inclusions from $N_{\text{cl}} = 10$ to $N_{\text{cl}} = 10^3$.

The upper panels of Figure 3 present the resulting maps of minimum aligned size a_{align} calculated in the xy -plane (left panel) and the xz -plane (right panel). The results illustrate the considerably small value of $a_{\text{align}} < 0.05 \mu\text{m}$, implying that circumstellar grains could easily achieve suprathermal rotation by strong stellar radiation fields from IK Tau and be effectively aligned with B-fields. However, a_{align} is higher along the equator with $\sim 0.05 \mu\text{m}$, which is shown in the lower panel of Figure 3 by a dashed black line. This is caused by the dipole field components perpendicular to radiation fields (i.e., $\mathbf{k} \perp \mathbf{B}$) at the equator, leading to the reduced RAT alignment efficiency and larger a_{align} . While in the polar region, $\mathbf{k} \parallel \mathbf{B}$, and the external grain alignment becomes more efficient, resulting in small $a_{\text{align}} \sim 5 - 10$ nm. And the grain alignment size decreases from $a_{\text{align}} \sim 10$ nm at $r \sim 100$ au to $a_{\text{align}} \sim 5$ nm at $r \sim 10000$ au (the lower panel of Figure 3, dashed black line), due to the reduced gas density in the outer region of IK Tau CSE.

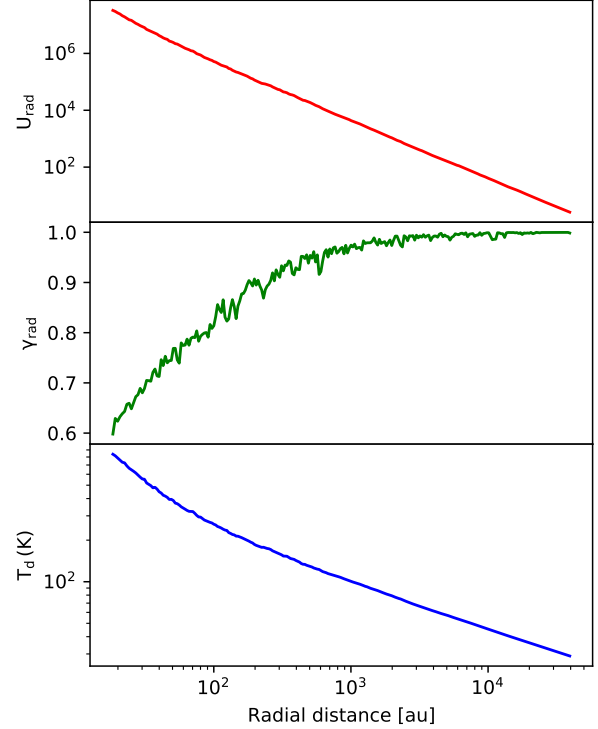


Figure 2. The distribution of radiation strength U_{rad} (top panel), the average of anisotropy degree γ_{rad} (middle panel) and dust temperature T_{d} (bottom panel) varying with the envelope distance.

For the maximum aligned size $a_{\text{max,JB}}^{\text{Lar}}$, one can see from the lower panel of Figure 3 (solid color lines) that, under the impact of luminous stellar radiation, most circumstellar dust could have fast Larmor precession with shorter timescale than the gas damping timescale. Consequently, they could achieve magnetic alignment by RATs efficiently with $a_{\text{max,JB}}^{\text{Lar}} = a_{\text{max}} = 0.5 \mu\text{m}$, even for the cases of PM and SPM grains.

4.2.2 Critical sizes for internal grain alignment by Barnett

$$\text{relaxation } a_{\text{max,aJ}}^{\text{high-J}}, a_{\text{max,aJ}}^{\text{low-J}}$$

Figure 4 shows the critical sizes having internal alignment for grains at high-J and low-J attractors, with the maximum size of $a_{\text{max,aJ}}^{\text{high-J}}$ (solid color lines) and $a_{\text{max,aJ}}^{\text{low-J}}$ (dashed color lines), considering different magnetic properties of PM and SPM grains. As can be seen, in the condition of strong radiation fields in IK Tau envelope, grains at high-J are easily achieved fast internal alignment, leading to $a_{\text{max,aJ}}^{\text{high-J}} = a_{\text{max}} = 0.5 \mu\text{m}$.

For grains at low-J attractors, one obtains $a_{\text{max,aJ}}^{\text{low-J}}$ decreases with increasing envelope distance, resulting from the reduction of gas randomization followed by the decrease in gas density (see the lower panel of Figure 1). In addition, the increase in magnetic susceptibility for SPM grains with high N_{cl} causes the increase in $a_{\text{max,aJ}}^{\text{low-J}}$ and the extension in the fast internal alignment region from the outer region

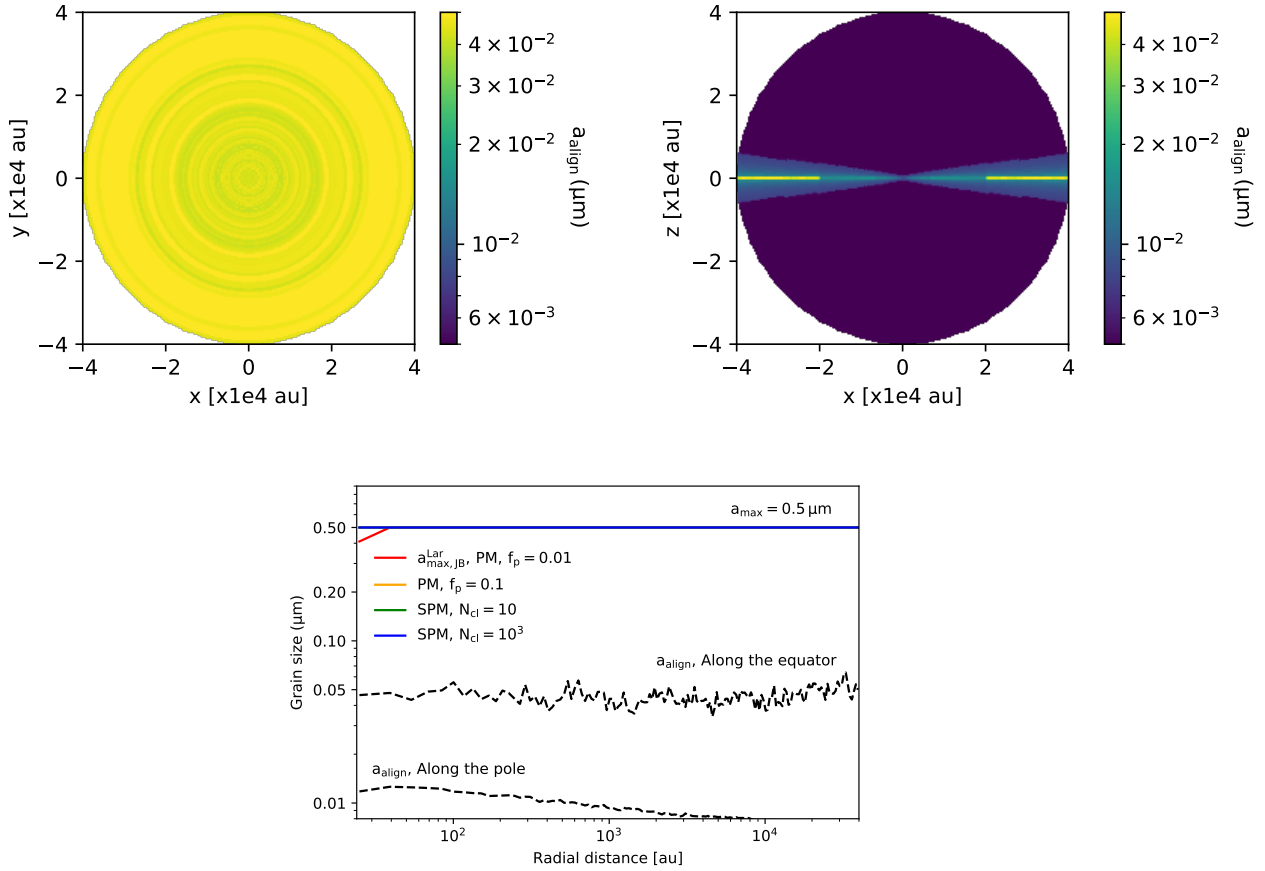


Figure 3. Upper panels: Maps of the minimum aligned size a_{align} calculated in the same xy -plane (left panel) and xz -plane (right panel). As being affected by stellar magnetic field geometry, the external alignment efficiency is reduced at the equator due to $\mathbf{k} \perp \mathbf{B}$, resulting in larger a_{align} . Lower panel: The variation of the minimum a_{align} (dashed black lines) and the maximum aligned sizes $a_{\text{max}}^{\text{Lar}}$ (solid color lines) as a function of the envelope distance for both PM and SPM grains with different levels of iron inclusions N_{cl} , assuming $\phi = 0.005$ and dust-to-gas ratio $M_{\text{d/g}} = 0.005$. Being exposed to luminous stellar radiation fields, most circumstellar dust could effectively achieve magnetic alignment by RATs.

of $r \sim 10000$ au to the inner region of $r \sim 100$ au of the IK Tau envelope.

4.2.3 Critical sizes for grain alignment by MRAT mechanism

$$a_{\text{max,JB}}^{\text{DG-0.5}}, a_{\text{max,JB}}^{\text{DG-1}}$$

Figure 5 illustrates the critical aligned sizes $a_{\text{max,JB}}^{\text{DG-1}}$ (dashed color lines) and $a_{\text{max,JB}}^{\text{DG-0.5}}$ (solid color lines) considering the contribution of magnetic relaxation in enhancing RAT alignment (i.e., MRAT mechanism). Even for PM grains with $f_p = 0.01$ and $f_p = 0.1$ (red and yellow lines), the alignment can be induced by strong stellar magnetic fields of 10 mG - 1 G within the inner region of $r < 500$ au, and subsequently, the effect of magnetic relaxation on grain alignment becomes efficient. At a larger envelope distance $r > 500$ au, both values of $a_{\text{max,JB}}^{\text{DG-1}}$ and $a_{\text{max,JB}}^{\text{DG-0.5}}$ drop significantly, corresponding to the decrease in magnetic field strength to 10 - 100 mG (see the lower panel of Figure 1).

As for the case of SPM grains with $N_{\text{cl}} = 10$ (green lines), the contribution of iron inclusions helps the MRAT mechanism happen at $r > 500$ au. And with the increasing level of iron inclusions to $N_{\text{cl}} = 10^3$ (blue lines), the active MRAT region can extend to further envelope distance of $r > 10000$ au.

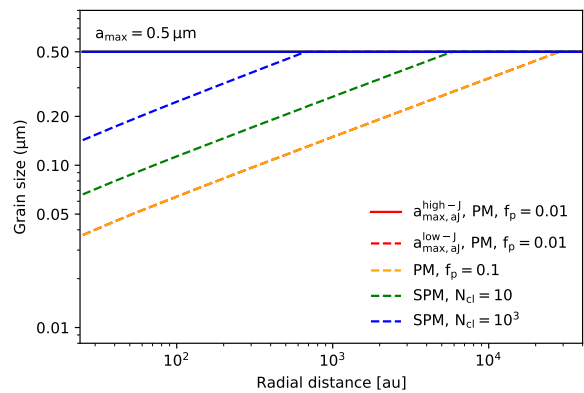


Figure 4. The variation of the maximum sizes of grains at high-J (solid color lines) and low-J attractors (dashed color lines) having fast internal alignment by Barnett relaxation, denoted by $a_{\text{max,aj}}^{\text{high-J}}$ and $a_{\text{max,aj}}^{\text{low-J}}$, for PM and SPM grains with various values of N_{cl} . Most grains at high-J attractors could have fast internal alignment with $a_{\text{max,aj}}^{\text{high-J}} = a_{\text{max}} = 0.5 \mu\text{m}$. Meanwhile, grains at low-J obtain thermal rotation by gas. Thus, $a_{\text{max,aj}}^{\text{low-J}}$ increases due to the decrease in gas randomization within the envelope distance.

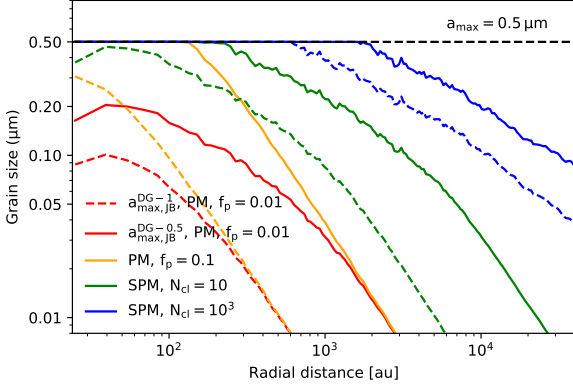


Figure 5. The variation of the maximum grain sizes having external alignment by MRAT mechanism, denoted by $a_{\max, \text{JB}}^{\text{DG}-1}$ (dashed color lines) and $a_{\max, \text{JB}}^{\text{DG}-0.5}$ (solid color lines), for PM and SPM grains. Under the effect of strong stellar magnetic field, the values of $a_{\max, \text{JB}}^{\text{DG}-1}$ and $a_{\max, \text{JB}}^{\text{DG}-0.5}$ are higher in the inner envelope $r < 500$ au. The impact of the MRAT mechanism extends from the inner to the outer region of the IK Tau envelope for SPM grains with increasing N_{cl} .

4.2.4 Critical disruption sizes by RAT-D

Figure 6 shows the maximum grain size after being disrupted by RATs a_{disr} (i.e., RAT-D mechanism, left panel) and the modified slope of grain size distribution (GSD) η (right panel), assuming varying values of $S_{\text{max}} = 10^6 - 10^{10}$ erg cm $^{-3}$. One can see that the impact of radiative torques from strong stellar radiation causes the fragmentation of large grains, resulting in the enhanced distribution of smaller grains with steeper $\eta < -3.5$ and smaller $a_{\text{disr}} < a_{\text{max}}$.

The variation of both a_{disr} and η within the envelope distance is associated with the joint effect of the spin-up by RATs and the spin-down by gas rotation. As shown in Figure 6, in the innermost region of $r \sim 18$ au, most grains are being disrupted by RAT-D with small a_{disr} and η , and then, these values slightly increase as a result of high gas density (i.e., $n_{\text{gas}} > 10^7$ cm $^{-3}$) causing efficient rotational damping by gas randomization. At a further distance of $r > 100$ au, the considerable decrease in gas density causes the enhanced rotational disruption by stellar radiation, resulting in a steady decrease in both values of grain disruption size a_{disr} and slope of GSD η .

Figure 6 also shows the dependency of RAT-D efficiency on grain internal structure in the IK Tau envelope. Porous grains with $S_{\text{max}} < 10^9$ erg cm $^{-3}$ are strongly being disrupted by RAT-D, and thus, an amount of smaller grains are enhanced (i.e., low a_{disr} and η). By contrast, grains with compact structure (i.e., $S_{\text{max}} > 10^9$ erg cm $^{-3}$) are difficult to be fragmented by RAT-D, leading to the survival of large grains with higher values of a_{disr} and η .

4.3 Dust polarization maps

From critical aligned sizes constrained by RAT alignment, we consequently model synthetic dust polarization with the implementation of the updated Rayleigh factor based on grain alignment properties in the updated version of POLARIS (see Giang et al. 2023). This section presents synthetic results of thermal dust polarization observed in far-IR/sub-mm wavelengths, considering the major effects on the polarization map: (1) inclination viewing angles, (2) magnetic properties of grains, and (3) rotational disruption by RATs.

4.3.1 Multi-wavelength polarization

Figure 7 illustrates synthetic polarization maps of the entire IK Tau CSE of 80000 au at optically thin wavelengths ranging from 53 μm to 870 μm . The large-scale maps are captured by a plane detector having 250×250 pixels placed at 265 pc from the central star to an observer on Earth, providing the spatial resolution of 320 au. The color code represents the polarization degree p (%), while black segments represent the pattern of polarization vector \mathbf{P} . We first consider the Ideal model in which all grains larger than the minimum aligned sizes a_{align} could achieve fast internal relaxation (i.e., $f_{\text{high-J}} = 1$) and perfectly align with stellar magnetic fields.

One can see when observing in sub-mm wavelengths (e.g., 870 μm and 450 μm), the polarization degree is higher in the outer region of $r > 10000$ au, which is mostly produced by the thermal emission of cold dust of $T_{\text{d}} < 100$ K (see the dust temperature profile in Figure 2). As decreasing to shorter wavelength bands (e.g., 53 μm and 89 μm), the maximum polarization degree shifts to the inner envelope of $r < 10000$ au, indicating the thermal emission by warm dust of $T_{\text{d}} > 100$ K in this region.

4.3.2 Effects of inclination angle

An important note is the major impact of inclination angles (i.e., θ_{incl} , the angle between the observed line-of-sight toward the source and the z -axis) on the observed stellar magnetic fields in the plane-of-sky, which directly affects the calculation of dust polarization in AGB envelopes. Figure 7 shows this effect on the dust polarization maps, both on polarization vector and polarization degree measured at optically thin wavelengths, assuming viewed at two main inclination angles: $\theta_{\text{incl}} = 10^\circ$ and $\theta_{\text{incl}} = 90^\circ$.

The upper panels of Figure 7 show the polarization maps observed in a face-on view (i.e., $\theta_{\text{incl}} = 10^\circ$) along x - and y -directions. The polarization vectors indicate a toroidal structure associated with the azimuthal structure of stellar magnetic fields in the xy -plane when rotating to 90 degrees (see the upper left panel of Figure 1). The polarization degree distributes uniformly with $p \sim 25 - 30$ % due to the projected components of B-fields mostly lying in the plane-of-sky, enhancing the polarization fraction in observation.

The lower panels of Figure 7 illustrate the resulting map in an edge-on-view (i.e., $\theta_{\text{incl}} = 90^\circ$) along x - and z -directions. The polarization vectors present a dipole structure along the x -axis, which is perpendicular to the dipole pattern of stellar magnetic fields in the xz -plane (see the upper right panel of Figure 1). The change in the curvature of dipole fields from the polar to the equator region results in the variation in the projected B-fields in the plane-of-sky. Subsequently, under the projection effect of magnetic field geometry, the polarization degree is higher at the equator and the outermost polar region of the IK Tau envelope of $r \sim 30000$ au with $p \sim 50$ %, while in the inner regions of $r < 30000$ au, p is lower with $\sim 30 - 40$ %, which is the impact of perpendicular components of stellar magnetic fields that reduces the resulting polarization degree.

4.3.3 Effects of iron inclusions

As discussed in the previous sections, dust polarization at far-IR/sub-mm regimes could trace the global magnetic fields of IK Tau with $\mathbf{P} \perp \mathbf{B}$ as most grains have both perfect internal and external alignment in the Ideal model. We then consider the Realistic models for PM and SPM grains, with the consideration of MRAT mechanism in the dust polarization calculation.

Figure 8 shows the large-scale map of the IK Tau envelope at

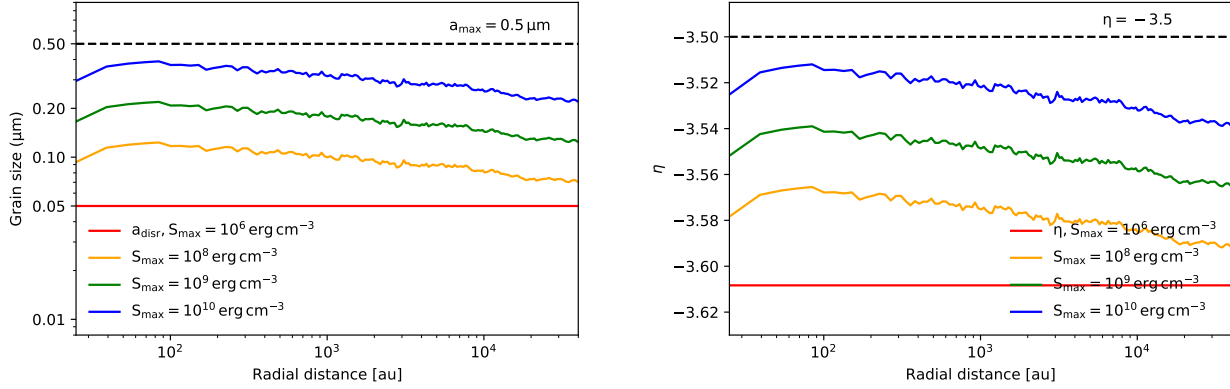


Figure 6. The variation of grain disruption size a_{disr} (left panel) and slope of grain size distribution η (right panel) with respect to the envelope distance for grains with $S_{\text{max}} = 10^6 - 10^{10} \text{ erg cm}^{-3}$. Radiative torques from stellar radiation could disrupt large grains into smaller species with $a_{\text{disr}} < a_{\text{max}} = 0.5 \mu\text{m}$ and steeper slope $\eta < -3.5$.

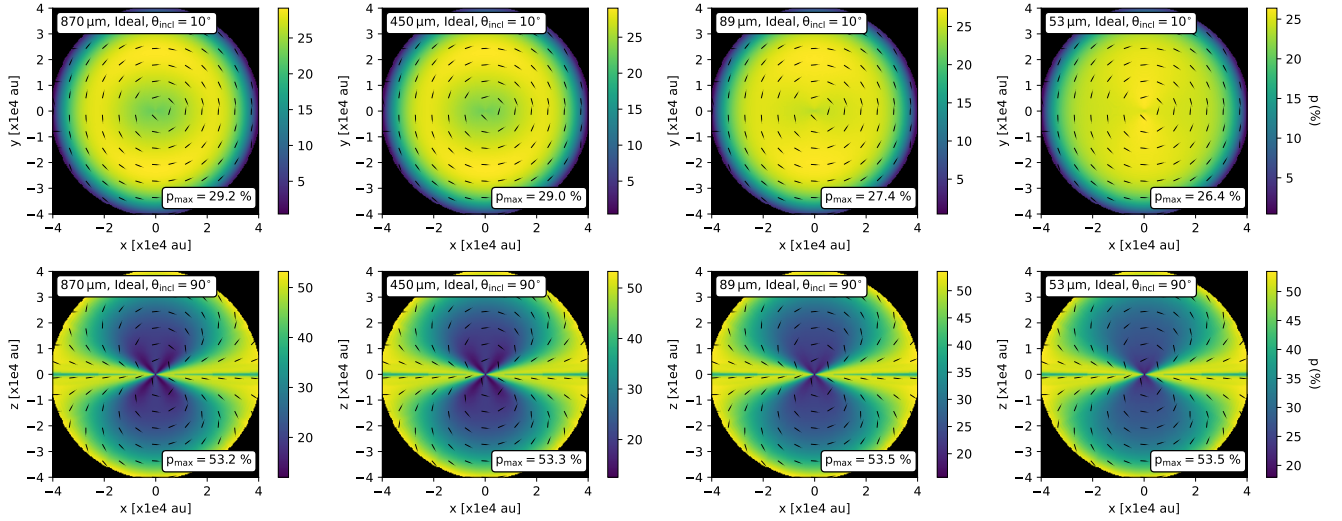


Figure 7. Multi-wavelength dust continuum polarization maps ($\lambda = 53 - 870 \mu\text{m}$) produced by the Ideal model (i.e., $a > a_{\text{align}}$ could align with B-fields) observed in face-on (i.e., $\theta_{\text{incl}} = 10^\circ$, top panels) and edge-on views (i.e., $\theta_{\text{incl}} = 90^\circ$, bottom panels). The color code illustrates the polarization fraction p (%), while black quiver lines show the pattern of polarization vector \mathbf{P} . The polarization degree shifts from thermal dust emission by cold dust in the outer envelope at longer wavelengths to thermal dust emission by warm dust in the inner envelope at shorter wavelengths.

$870 \mu\text{m}$ in the face-on (upper panels) and edge-on observations (lower panels), considering the realistic models of PM grains with $f_p = 0.1$ (second column), and SPM grains with $N_{\text{cl}} = 10$ (third column) and $N_{\text{cl}} = 10^3$ (last column). For PM grains, the polarization fraction is lower with $p \sim 14 - 26\%$ due to low magnetic susceptibility. For SPM grains, the contribution of iron inclusions enhances the magnetic susceptibility. As a result, the polarization degree increases with increasing the level of iron inclusions locked inside dust grains to $p \sim 22 - 47\%$ for SPM grains with $N_{\text{cl}} = 10^3$.

Figure 9 shows similar, but zooming in the small-scale region of 1000 au. For PM grains, the higher p is mostly concentrated within the inner envelope of $r < 100$ au, which is a result of the enhanced MRAT alignment due to strong stellar magnetic field strength in this region (see Figure 5). For SPM grains, the incorporation of iron into dust grains causes the extension of the active MRAT region as

increasing N_{cl} . Consequently, the polarization degree becomes more extended to the outer envelope of $r > 500$ au of the IK Tau CSE.

4.3.4 Effects of RAT-D

Later, we consider the implication of the RAT-D mechanism for observing dust polarization in AGB envelopes. The modification of grain size distribution by RAT-D could considerably impact the resulting polarization maps, which will be described in this section.

Figure 10 and 11 shows the RAT-D effects on the $870 \mu\text{m}$ synthetic dust polarization for the large-scale map of the IK Tau envelope and small-scale map of the central region of 1000 au, respectively, assuming being observed at $\theta_{\text{incl}} = 10^\circ$. We examine the dependence of RAT-D on the magnetic properties of grains in both Ideal and Realistic models for PM and SPM materials. We consider the disruption for grains with $S_{\text{max}} = 10^6 \text{ erg cm}^{-3}$ (second row),

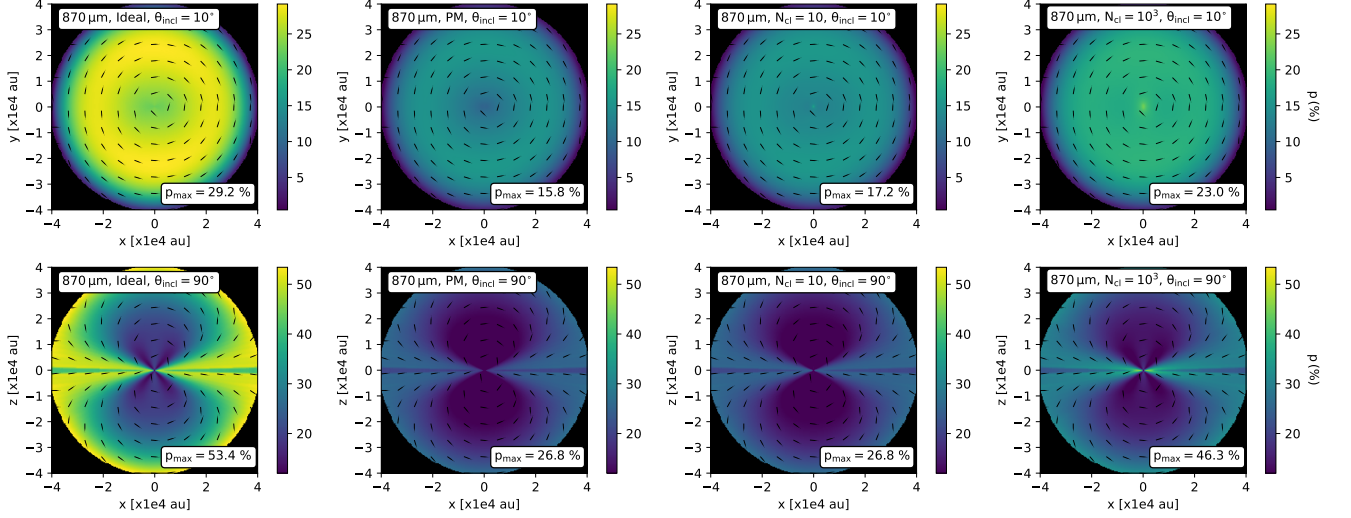


Figure 8. Synthetic dust polarization maps observed at $870\ \mu\text{m}$ with two inclination angles: $\theta_{\text{incl}} = 10^\circ$ and $\theta_{\text{incl}} = 90^\circ$, in the envelope scale, produced by PM and SPM grains with different levels of N_{cl} . The polarization patterns change from azimuthal to dipole structure as increasing θ_{incl} , corresponding to the modification of stellar magnetic field geometry in different observed views. The polarization degree is lower for the case of PM grains, and it increases with increasing N_{cl} for SPM grains due to higher magnetic susceptibility.

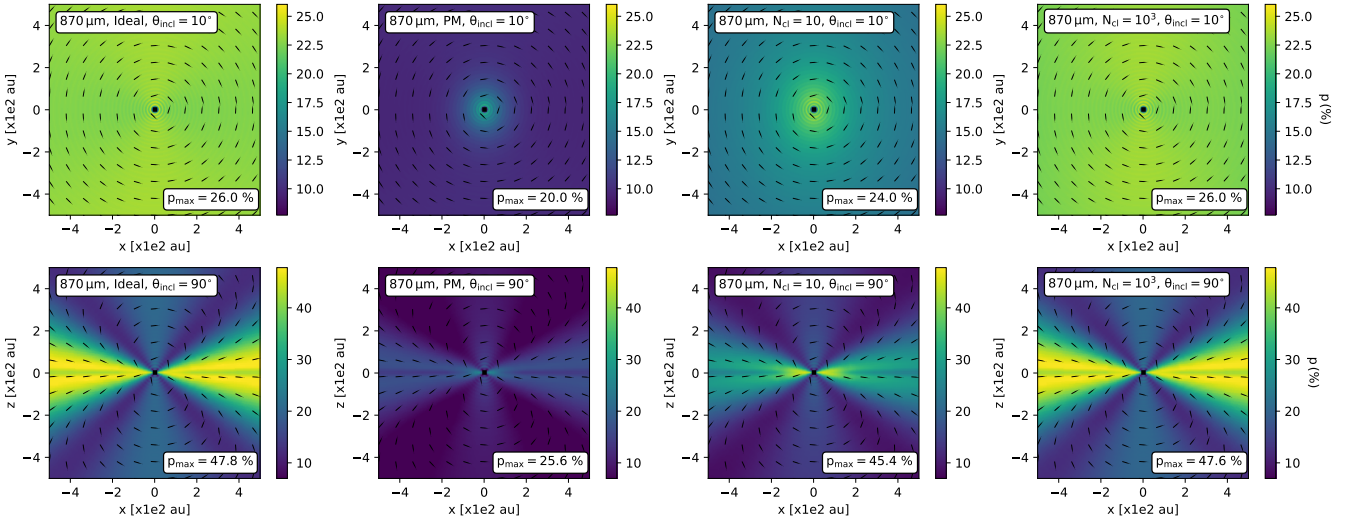


Figure 9. Similar to Figure 8 but in the small central region scale of 1000 au. The polarization degree extends from the inner region of $r < 100$ au to the outer region of $r > 500$ au for PM and SPM grains with higher levels of iron inclusion as a result of the increased contribution of the MRAT mechanism (see Figure 5).

$S_{\text{max}} = 10^8$ erg cm $^{-3}$ (third row) and $S_{\text{max}} = 10^{10}$ erg cm $^{-3}$ (last row), while the non-disrupted case is added for comparison (first row).

It is clearly seen that, as the RAT-D happens, large grains are fragmented by RATs from stellar radiation, resulting in the enhancement of smaller grains and a narrower GSD of silicate dust in the IK Tau envelope. As a result, the polarization degree is reduced with lower p . For instance, in the Ideal model (first column of Figure 10), $p_{\text{max}} \sim 26.8\%$ for grains with $S_{\text{max}} = 10^6$ erg cm $^{-3}$, while $p_{\text{max}} \sim 29.2\%$ in the case of no disruption.

The decrease in polarization fraction $p(\%)$ also depends on the internal structure of grains as being disrupted by RATs. Porous grains

undergo stronger disruption by stellar radiation, leading to the abundance of smaller grains (i.e., narrower GSD). Hence, the polarization degree becomes lower for grains with lower S_{max} . Meanwhile, compact grains with higher S_{max} are hard to be disrupted by RAT-D, resulting in the remaining of large grains (i.e., broader GSD) and higher p . As an example of the polarization maps in the Ideal model, $p_{\text{max}} \sim 26.8\%$ for grains with $S_{\text{max}} = 10^6$ erg cm $^{-3}$, while this value can be $\sim 28.8\%$ for grains with $S_{\text{max}} = 10^{10}$ erg cm $^{-3}$. This effect occurs in the entire envelope from the inner to the outer regions, which is shown in both Figure 10 and 11.

On the other hand, for PM grains, the results show a slight increase in polarization fraction $p(\%)$ for grains with lower S_{max} when ob-

served in the inner region of $r < 500$ au (second column in Figure 11). This is caused by the joint effect of RAT-D and MRAT mechanism, described by the profiles of $a_{\text{max,JB}}^{\text{DG}-1}$ and a_{disr} in Figure 5 and 6, respectively. A higher fraction of porous grains (i.e., low S_{max} and a_{disr}) constrained by RAT-D have perfect alignment by MRAT in the more extended region of $r < 500$ au (i.e., wider MRAT region), compared with a lower fraction of large compact grains (i.e., high S_{max} and a_{disr}) being enhanced by MRAT in the region of $r < 100$ au (i.e., narrower MRAT region). Therefore, the total polarization degree produced by PM grains is higher for grains with lower S_{max} . For instance, $p_{\text{max}} \sim 22.6\%$ and $\sim 21.6\%$ for grains with $S_{\text{max}} = 10^6$ erg cm $^{-3}$ and 10^{10} erg cm $^{-3}$, respectively.

This features shifts to the outer envelope of $r > 10000$ au for the polarization produced by SPM grains with embedded iron, as shown in the large-scale maps (third and last columns of Figure 10). It is associated with the enhancement of MRAT for SPM grains with increasing N_{cl} to the outer envelope of $r > 10000$ au (Figure 5). By contrast, in the inner envelope of $r < 500$ au (third and last columns of Figure 11), the effect of RAT-D is dominant, and the polarization induced by SPM grains decreases with decreasing value of S_{max} .

4.4 The p-I relationship

Figure 12 shows the variation of the $870 \mu\text{m}$ polarization fraction $p(\%)$ with respect to the normalized intensity I/I_{max} , where I_{max} is the maximum intensity produced by thermal dust emission in the innermost region of the IK Tau CSE, assuming observed at $\theta_{\text{incl}} = 10^\circ$ (i.e., face-on view). The normalized intensity I/I_{max} is calculated at each radial distance r along the x -axis (upper panels) and y -axis (lower panels) of the plane-of-sky, which is added in the top x -axis of Figure 12. We analyze both observations in the large-scale envelope of 80000 au (left panels) and the small-scale central region of 1000 au (right panels). Solid color lines represent the polarization degree p for Realistic models of PM and SPM grains, while that for Ideal case is plotted by a dashed black line for comparison.

As can be seen, for both calculations along the x - and y -axis, the polarization is significantly low with $p \sim 5 - 10\%$ in the outermost envelope of $r > 30000$ au. Toward the central star with $r < 30000$ au, p increases to the uniform values of $\sim 25 - 30\%$ as previously illustrated in the polarization maps in the upper panels of Figure 7, which is mainly enhanced by the projected components of the stellar magnetic field lying in the plane-of-sky observed in the xy -plane (see the upper left panel of Figure 1).

Figure 13 shows similar results as Figure 12, but in the edge-on view (i.e., $\theta_{\text{incl}} = 90^\circ$), taking the calculation along the x -axis (i.e., along the equator region, upper panels) and the z -axis (i.e., along the polar region, lower panels). At the equator, the radiation fields are perpendicular to the magnetic fields; therefore, the effect of magnetic field geometry on dust polarization is negligible. Hence, for the Ideal model, the main result is produced by the alignment of large grains with $a_{\text{align}} \sim 0.05 \mu\text{m}$ in the equator region of IK Tau envelope (the lower panel of Figure 3) with $p \sim 40\%$. Along the z -axis, the polarization is affected by the geometry of the dipole magnetic fields (see the upper right panel of Figure 1). The magnetic field lines become more curved when moving to the inner envelope of $r \sim 500 - 10000$ au. The B-field vectors become perpendicular to the plane-of-sky when moving to the inner region, causing the decrease in $p \sim 50\%$ at $r > 30000$ au to $p \sim 20\%$ at $r < 30000$ au, similar to the illustration in the polarization map in the lower panels of Figure 7 for the Ideal case.

One crucial factor that we emphasize is the effects of the magnetic properties of dust grains on the relationship $p - I/I_{\text{max}}$. As shown

in both Figure 12 and 13, one obtains that the polarization degree produced by PM grains is considerably lower with $p < 15\%$ due to the lower magnetic susceptibility. In comparison with the uniform value of p in the Ideal model within $r \sim 500 - 10000$ au, the polarization fraction decreases slightly as a result of a large proportion of grains at low-J attractors having low internal relaxation (right panel of Figure 4). In the inner region of $r < 500$ au, the contribution of magnetic relaxation in enhancing RAT alignment is significant with a high portion of grains at high-J attractors, leading to the increases in p with increasing iron fraction inside dust grains. For SPM grains with iron inclusions, the profiles $p - I/I_{\text{max}}$ illustrate the extension of polarization degree to the outer envelope of $r > 10000$ au similar to what obtains in the lower panel of Figure 9, corresponding to the enhanced contribution of the MRAT mechanism with increasing N_{cl} .

Figure 14 shows the mean polarization degree p obtained at $870 \mu\text{m}$ with varying I/I_{max} calculated within the ring located at the projected distance d_{proj} , with the radius of $d_{\text{resol}} = 320$ au for the large-scale map of the envelope (left panels) and $d_{\text{resol}} = 4$ au for the small-scale map of the central region of 1000 au (right panels). We take into account both face-on (upper panels) and edge-on observations (lower panels) for comparison. Generally, the magnetic field morphology impacts the resulting polarization degree mainly in the outer envelope of $d_{\text{proj}} > 10000$ au. In the inner envelope of $d_{\text{proj}} < 500$ au, the variation of p is affected by the alignment properties of grains, with the enhancement of polarization degree induced by MRAT for grains with higher levels of iron at $d_{\text{proj}} < 500$ au.

The RAT-D mechanism is taken into consideration in the analysis of the variation of the averaged p with increasing I/I_{max} observed at $\theta_{\text{incl}} = 10^\circ$, as illustrated in Figure 15. We consider the RAT-D effect on grains with varying $S_{\text{max}} = 10^6 - 10^{10}$ erg cm 3 (solid color lines), while the case without disruption is plotted in the dashed black line for comparison. One can see in the Ideal model (upper left panels of Figure 15) the polarization degree p decreases due to smaller grains being produced by RAT-D. And the polarization degree becomes lower for grains with porous structure (i.e., low S_{max}), compared with grains with compact structures (i.e., high S_{max}) and higher p .

By contrast, in the Realistic model produced by PM grains (upper right panels of Figure 15), the results show an opposite trend which p tends to increase with decreasing S_{max} in the inner envelope of $d_{\text{proj}} < 500$ au. This is a result of a high proportion of small porous grains having efficient external alignment by MRAT (Figure 5 and 6), thus, enhancing the polarization degree. Meanwhile, a small portion of large compact grains achieves MRAT alignment within the narrower region of $d_{\text{proj}} < 500$ au, resulting in lower p . In the outer envelope of $d_{\text{proj}} > 10000$ au, grains are mostly aligned by RATs. Hence, the polarization depends mostly on the impact of RAT-D on internal grain structure, with the decrease in $p(\%)$ for grains with porous structure.

The lower panels of Figure 15 show the results produced by SPM grains with N_{cl} . As changing the levels of iron inclusions from 10 to 10^3 , the feature of increasing p for grains with lower S_{max} shifts from the inner region of $d_{\text{proj}} < 500$ au to the outer region of $d_{\text{proj}} > 10000$ au, resulting from the abundance of grains at high-J attractors due to the enhanced grain alignment efficiency by MRAT along the envelope distance (Figure 5). Nevertheless, for SPM grains with high $N_{\text{cl}} = 10^3$, the polarization is primarily affected by RAT-D at $d_{\text{proj}} < 500$ au, leading to the reduction of p with decreasing S_{max} .

4.5 The polarization spectrum $p(\lambda)$

We investigate the polarization spectrum produced by aligned circumstellar grains in AGB envelopes in the range of optically thin

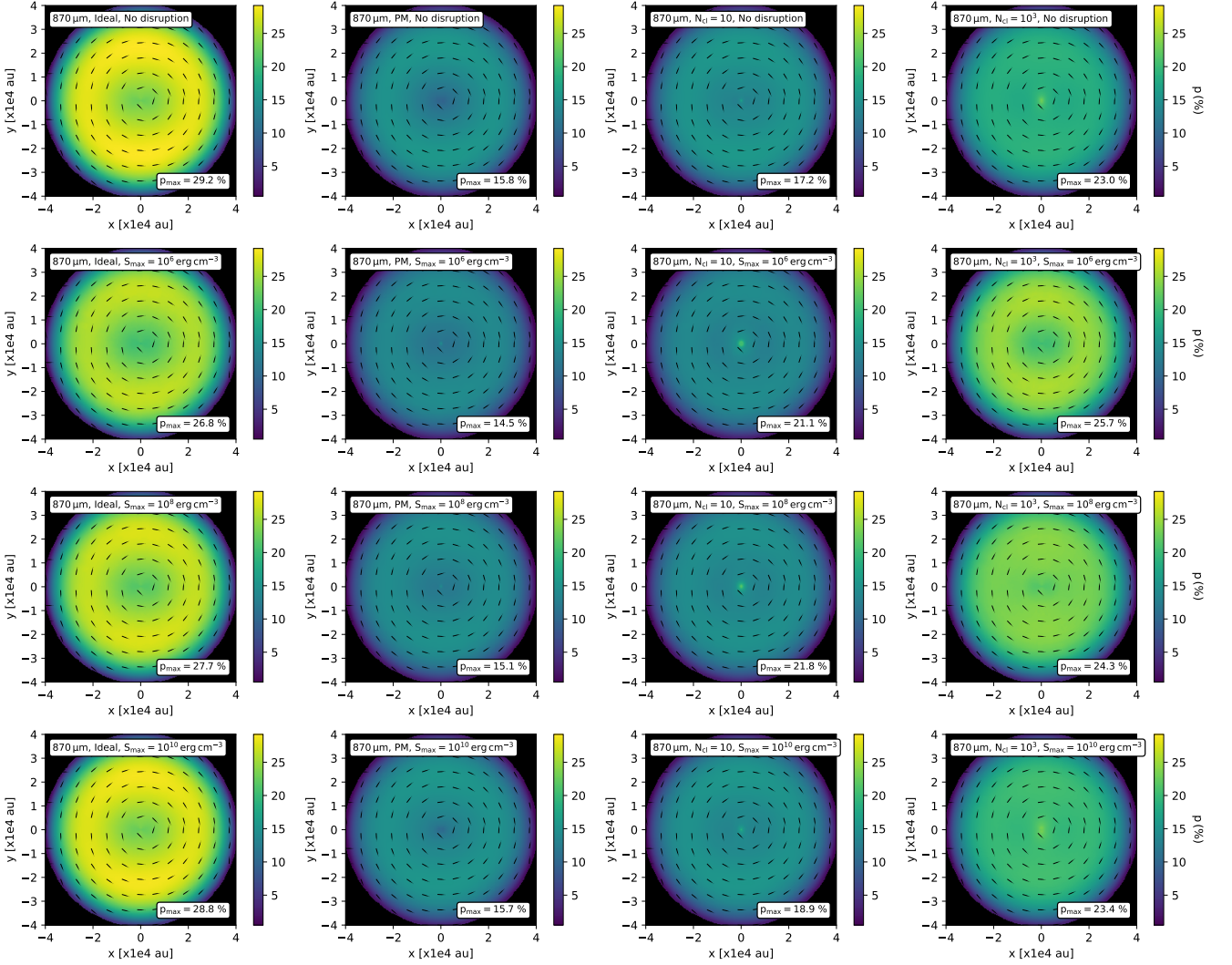


Figure 10. Synthetic dust polarization maps observed in the face-on view (i.e., $\theta_{\text{incl}} = 10^\circ$) at $870 \mu\text{m}$ produced by the Ideal and Realistic models for PM and SPM grains with $N_{\text{Cl}} = 10 - 10^3$, considering two configurations: no disruption (first row) and disruption for different grain internal structures with $S_{\text{max}} = 10^6 \text{ erg cm}^{-3}$ (second row), $S_{\text{max}} = 10^8 \text{ erg cm}^{-3}$ (third row) and $S_{\text{max}} = 10^{10} \text{ erg cm}^{-3}$ (last row). In the outer envelope of $r > 10000 \text{ au}$, the impact of the RAT-D mechanism effectively reduces the polarization degree for PM grains with porous structure. However, the joint contribution of RAT-D and MRAT causes the inverse effect, with the increase in p for SPM grains with lower S_{max} .

wavelengths from $25 \mu\text{m}$ to $870 \mu\text{m}$, as shown in Figures 16 and 17. The results are calculated in both the inner and the outer region of the IK Tau CSE, assuming the beam sizes of 30 au and 300 au , respectively. Compared with the model Ideal plotted by the dashed black line, we consider the spectrum produced by both PM and SPM grains as illustrated in solid color lines.

Figure 16 shows the results of the polarization spectrum in the face-on observation (i.e., $\theta_{\text{incl}} = 10^\circ$) at $d_{\text{proj}} = 100 \text{ au}$ (left panel) and $d_{\text{proj}} = 10000 \text{ au}$ (right panel). In general, the spectrum arises from the thermal emission of aligned grains with $a_{\text{align}} \sim 0.05 \mu\text{m}$ in the equator region with $\mathbf{k} \perp \mathbf{B}$ (the lower panel of Figure 3). The spectrum calculated in the inner envelope of $d_{\text{proj}} = 100 \text{ au}$ reaches a peak at the short wavelength of $\lambda \sim 50 \mu\text{m}$ and decreases gradually, which is from the thermal emission of warm dust near the central star. Moving far from the central star to $d_{\text{proj}} = 10000 \text{ au}$, the spectrum feature shows the continuous increase of p to uniform

values at $\lambda > 50 \mu\text{m}$, mostly from the thermal emission by cold dust located in the outer region of the IK Tau CSE.

Figure 17 shows the same but in the edge-on observations (i.e., $\theta_{\text{incl}} = 90^\circ$). In the inner envelope of $d_{\text{proj}} = 30 \text{ au}$ (left panel), the alignment of large grains of $a_{\text{align}} \sim 0.05 \mu\text{m}$ at the equator region strongly influences the polarization spectrum with the increase in $p(\%)$ increases toward the long wavelength regimes of $\lambda > 50 \mu\text{m}$. In the outer region of $d_{\text{proj}} = 10000 \text{ au}$ (left panel), the spectrum is dominantly induced by the alignment of small grains of $a_{\text{align}} \sim 5 - 10 \text{ nm}$ in the polar regions due to the effect of stellar magnetic field geometry with $\mathbf{k} \parallel \mathbf{B}$ that directly enhances the RAT alignment efficiency (Figure 3). As a result, the polarization fraction $p(\%)$ tends to increase toward the short wavelength regimes of $\lambda < 50 \mu\text{m}$.

The effects of iron inclusions on the polarization spectrum are considered in Figures 16 and 17. In the Realistic model of PM grains, the polarization spectrum is significantly lower than that in the Ideal case with $p < 15\%$ due to low magnetic susceptibility. In the Realistic

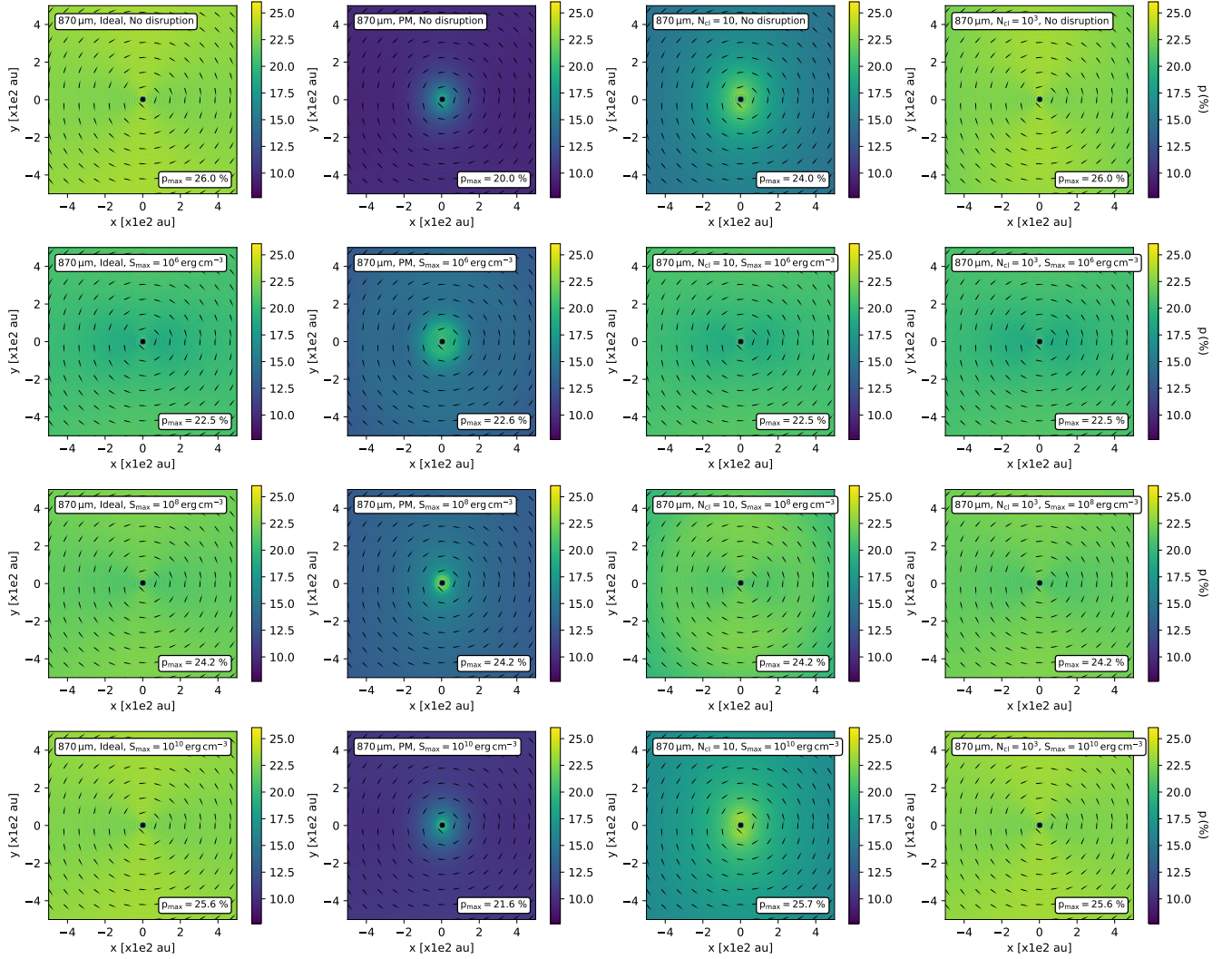


Figure 11. Same as Figure 10 but focusing on the inner region of 1000 au. In this region, the polarization degree produced by PM grains with porous structure (i.e., lower S_{\max}) is being enhanced due to the combined effects of RAT-D and MRAT. Meanwhile, the polarization degree induced by SPM grains is mainly affected by the RAT-D, resulting in the decrease in p for porous grains.

models of SPM grains with increasing level of N_{cl} , the polarization degree tends to increase to $p \sim 20 - 25\%$ for SPM grains with $N_{\text{cl}} = 10^3$, which is a result of the enhanced magnetic susceptibility caused by the presence of embedded iron inside dust grains.

Figure 18 concentrates on the effects of the RAT-D mechanism in modifying the polarization spectrum, calculating for grains with different values of S_{\max} . The polarization curve for the non-disrupted grains is added for comparison. In the Ideal case (first row), one obtains the reduction of polarization degree in the calculation at both $d_{\text{proj}} = 100$ au (left panel) and $d_{\text{proj}} = 10000$ au (right panel), resulting from a large amount of small grains produced by RAT-D. And the RAT-D mechanism is more efficient for porous grains (i.e., low S_{\max}); consequently, the polarization degree calculated in the entire spectrum is lower than that produced by large compact grains (i.e., high S_{\max}).

In the case of PM grains (second row), Figure 18 illustrates the difference in the resulting polarization spectrum at the inner and the outer region of the IK Tau CSE. At $d_{\text{proj}} = 100$ au, the results

show the flipping in the polarization spectrum with higher p for lower values of S_{\max} due to the combined effects of the RAT-D and MRAT mechanism on enhancing grain alignment efficiency of small porous grains constrained by RAT-D (Figure 5 and 6). Meanwhile, at $d_{\text{proj}} = 10000$ au, the RAT-D mechanism mainly contributes to reducing the polarization degree, resulting in lower p with decreasing S_{\max} .

Turning to the models of SPM grains, the results show the modification from the flipping of polarization spectrum in the inner region of $d_{\text{proj}} = 100$ au for SPM grains with $N_{\text{cl}} = 10$ (third row) to the flipping observed at the outer region of $d_{\text{proj}} = 10000$ au for SPM grains with $N_{\text{cl}} = 10^3$ (last row) due to the extended contribution of MRAT regions to the outer envelope for SPM grains with high levels of iron (Figure 5). And as increasing N_{cl} to 10^3 , the polarization spectrum calculated in the inner region of $d_{\text{proj}} = 100$ tends to be reduced mainly by the RAT-D effect with lower p for porous grains with low S_{\max} .

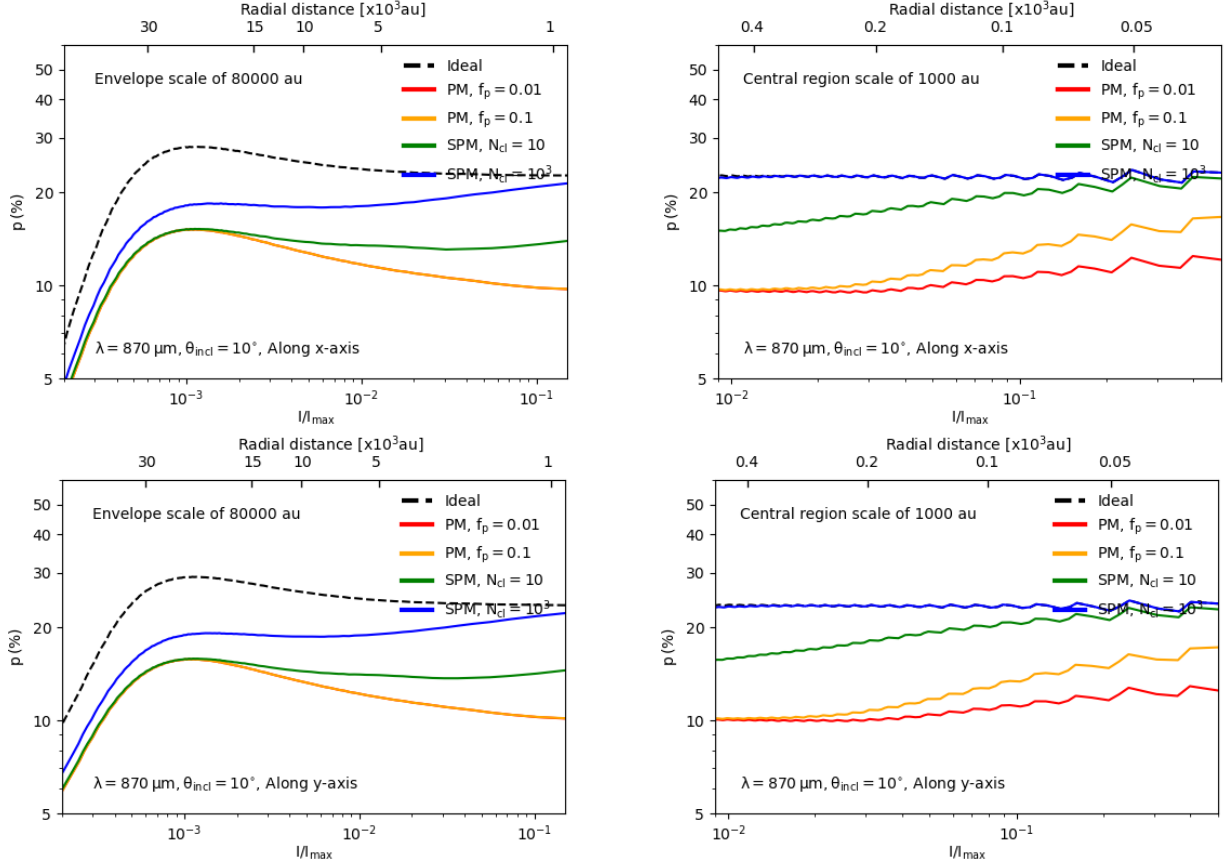


Figure 12. The variation of polarization fraction p (%) at $870\ \mu\text{m}$ with the normalized intensity I/I_{max} for both Ideal (dashed black line) and Realistic cases of PM and SPM grains (solid color lines) in the face-on view (i.e., $\theta_{\text{incl}} = 10^\circ$), considering the observations in the envelope scale of 80000 au (left panels) and the central region scale of 1000 au (right panels). Both observations along x - (upper panels) and y -axis (bottom panels) show the increase in p within the region of $r \sim 10000 - 30000$ au as a result of the B-field components lying in the plane-of-sky. Additionally, p increases for PM and SPM grains with higher levels of iron resulting from higher magnetic susceptibility and the extended MRAT effects.

5 DISCUSSION

5.1 Grain alignment properties in evolved star envelopes

The study of internal and external grain alignment by RATs is vital for examining how we reliably extract the morphology of stellar magnetic fields by using thermal dust polarization in astronomical environments. Both the internal and external alignment efficiencies of grains depend greatly on the environmental conditions (e.g., radiation, gas density, and magnetic fields) and the grain properties (e.g., mineralogy, size distribution, and magnetic properties). In the diffuse ISM environment and dense MCs, small PM grains of $a < 1\ \mu\text{m}$ could sufficiently achieve perfect internal alignment with the Barnett relaxation faster than gas randomization and efficient external alignment by RATs (Lazarian & Hoang 2007; Andersson et al. 2015). However, this is not the case in dense environments such as protostellar cores and disks in which very large grains (VLGs) of $a > 10\ \mu\text{m}$ with PM materials formed and grown inside could not be effectively aligned with B-fields due to the strong gas damping with high density (i.e., $n_{\text{gas}} > 10^7\ \text{cm}^{-3}$). The detailed numerical studies of Hoang (2022) and Hoang et al. (2022) showed that the presence of iron in the form of clusters could enhance the external alignment by magnetic relaxation, and therefore, only SPM grains could be sufficiently aligned with the local B-fields. The authors also showed that the embedded iron could help grains at high-J attractors have efficient internal alignment rather than those at low-J attractors

with slow thermal rotation, which was confirmed by the modeling in low-mass protostellar cores using the updated POLARIS by Giang et al. (2023).

Our detailed modeling of RAT alignment in the IK Tau envelope shows that in terms of internal alignment (Section 4.2.2), silicate grains at high-J attractors can easily have fast internal Barnett relaxation by RATs from the strong radiation from the central AGB star, even for PM and SPM materials. Hence, they can sufficiently have the perfect internal alignment. Nevertheless, for grains at low-J attractors (dashed color lines in Figure 4), the increasing gas randomization with decreasing envelope distance causes the reduction of the Barnett relaxation efficiency. As a result, the fast internal relaxation of PM grains rotating subthermally by gas collision can only happen in the outer envelope of $r > 10000$ au, while the existence of embedded iron inclusions in SPM grains helps them achieve effective internal relaxation in the inner envelope of $r < 500$ au.

As we also present in the modeling of external grain alignment in evolved star envelopes using RAT theories (Section 4.2.1 and 4.2.3), silicate grains with the radius of $a \lesssim 0.5\ \mu\text{m}$ can have effective external alignment by RATs induced by luminous stellar radiation (Figure 3). Additionally, we find that the presence of a strong magnetic field of $B \sim 10\ \text{mG}$ to $1\ \text{G}$ is responsible for the efficient magnetic relaxation for PM silicate grains, which enhances the population of grains at high-J with fast internal relaxation in the inner region of $r < 500$ au and strengthens the external alignment by RATs (Figure

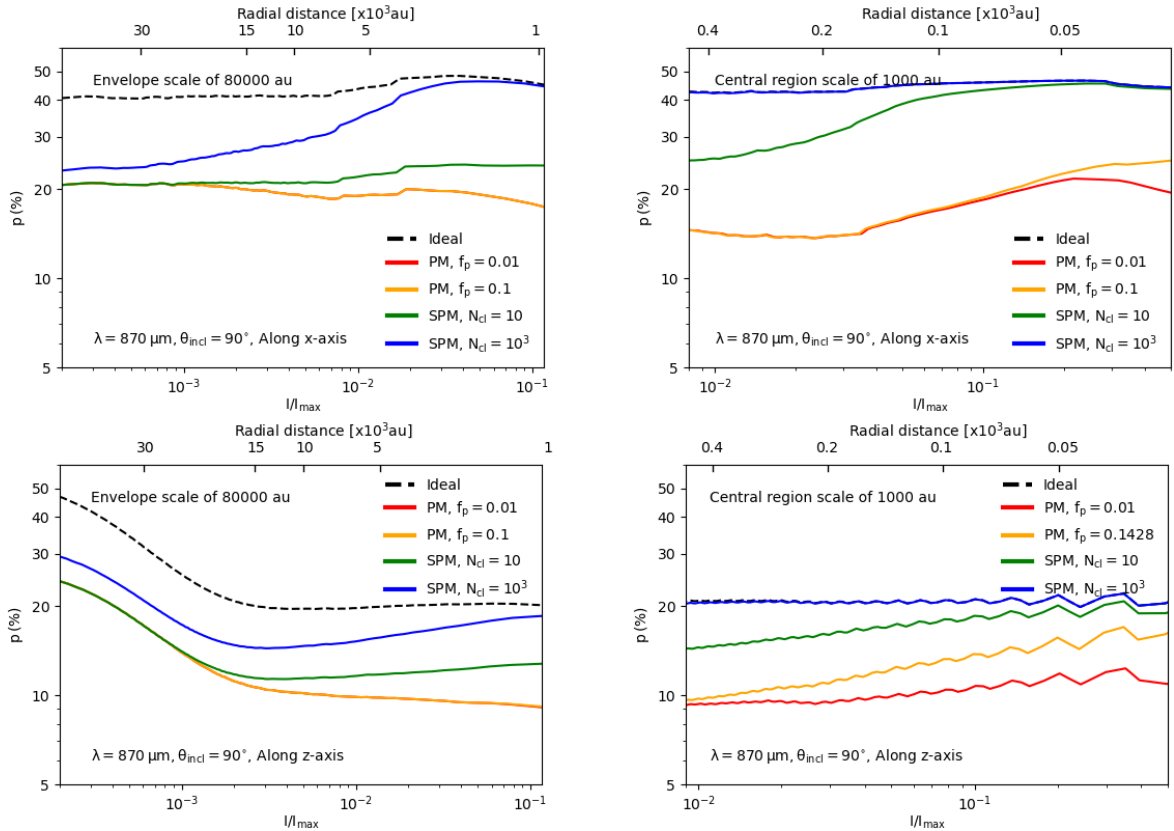


Figure 13. Similar results of Figure 12 but considering the observations in the edge-on view (i.e., $\theta_{\text{incl}} = 90^\circ$). Along the x-axis (upper panels), the polarization fraction increases toward the central star caused by the increased grain alignment by RATs. On the other hand, along the z-axis (lower panels), p (%) decreases significantly, resulting from the change in the curvature of the stellar dipole magnetic fields.

5). This effect is more significant for PM and SPM grains with a higher abundance of embedded iron (i.e., high f_p and N_{cl}), allowing them to have perfect alignment with the ambient B-fields in the outer envelope of $r > 10000$ au with $f_{\text{high-J}} = 1$. The internal and external alignment properties of silicate grains are strongly related to the potential of reproducing the large-scale magnetic field morphology in AGB envelopes, which will be discussed in Section 5.5.

5.2 Roles of embedded iron in enhancing polarization degree in AGB envelopes

The existence of iron incorporated into grains is a key factor in verifying dust polarization observations in very dense environments such as protostellar cores/disks in the early phase of stellar formation and evolved star envelopes in the late phase of stellar evolution. In protostellar environments, the modeling of dust polarization in the low-mass protostellar cores using POLARIS by Giang et al. (2023) showed the increase in polarization fraction p (%) up to $\sim 40\%$ produced by VLGs with high levels of iron inclusions, which is consistent with the SMA and ALMA observations of protostellar cores/disks with high polarization degree (Hull et al. 2014; Cox et al. 2018). This effect of embedded iron inside grains on enhancing polarization degree was also found in the thermal dust polarization observations with $p \sim 20\% - 30\%$ induced by micron-sized grains $a < 1 \mu\text{m}$ in massive filaments (Ngoc et al. 2023).

In evolved star environments, using the updated version of POLARIS, we show the enhanced alignment by MRAT is a major cause of the increase in polarization degree produced by small PM sub-

micron grains $a < 0.2 \mu\text{m}$ (see Figure 5) toward the inner region of $r < 500$ au to $\sim 10\%$, as illustrated in the profiles of $p - I/I_{\max}$ (see Section 4.4). The increasing fraction of iron inside PM grains can produce a more efficient alignment by MRAT for larger grains and induce a higher polarization degree within 100 au (see the right panels of Figure 12, 13 and 14). And for SPM grains with high levels of iron inclusion, a high amount of grains at high-J attractors is populated by the MRAT, as we discussed previously in Section 5.1. As a result, this considerably enhances the overall polarization degree in the entire envelope, possibly up to $\sim 20 - 40\%$ in the inner region of $r < 500$ au and extends to the outer envelope of $r > 10000$ au following the extended impacts of MRAT mechanism. The increasing polarization degree concerning the increasing amount of iron inclusions in SPM grains is also presented in the prediction of the polarization spectrum at far-IR/sub-mm, as illustrated in Figures 16 and 17. This raises an open approach to constraining the level of iron locked inside grains via dust polarimetry in AGB envelopes, which will be discussed in Section 5.6.

5.3 Roles of RAT-D in modifying dust polarization degree in AGB envelopes

The rotational disruption from stellar radiation on the properties of circumstellar dust has a major impact on the observational properties of evolved stars. Tram et al. (2020) showed that the RAT-D effects are independent of grain mineralogy and could be applied in the environments of both C-rich and O-rich AGB envelopes. The authors constrained the upper limit of grain size distribution by RAT-D and

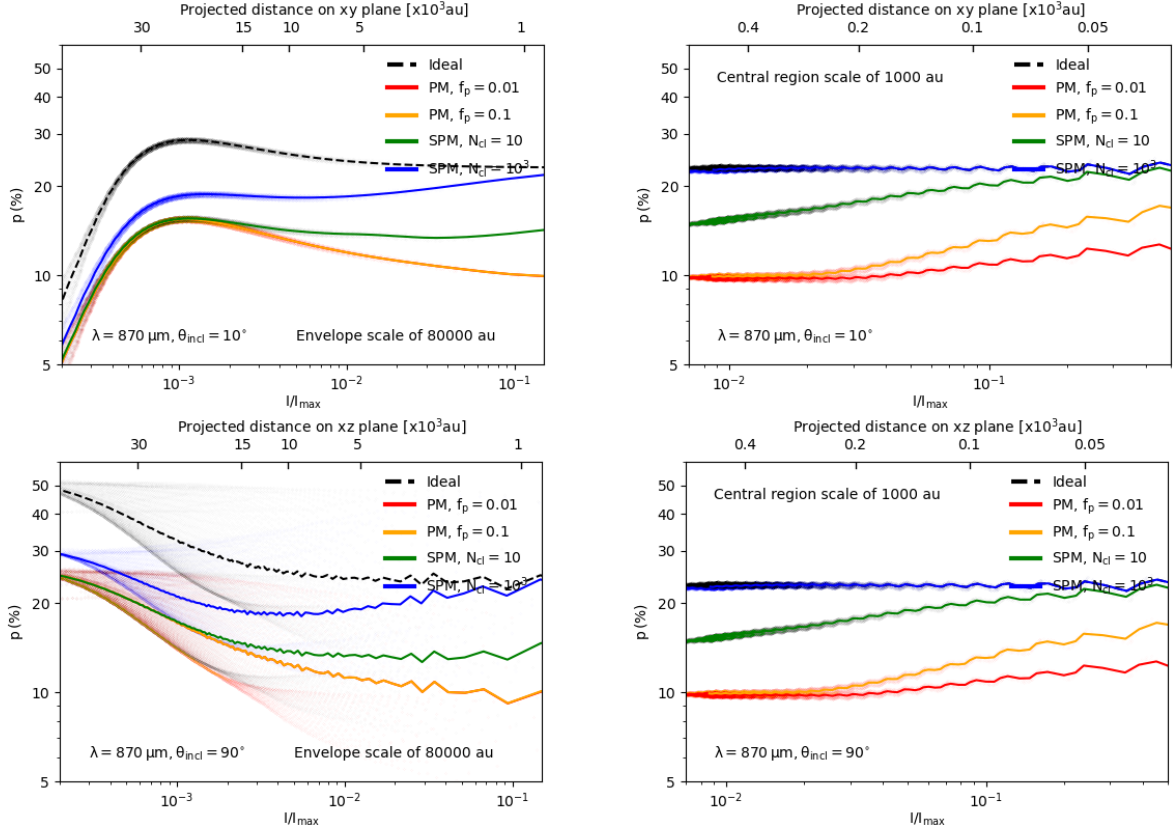


Figure 14. The averaged intensity-dependent polarization fraction $p - I/I_{\max}$ at each projected distance d_{proj} in the observed plane-of-sky, assuming observed at $\theta_{\text{incl}} = 10^\circ$ (upper panels) and $\theta_{\text{incl}} = 90^\circ$ (lower panels). The effects of stellar magnetic field geometry on dust polarization mostly in the outer envelope of $d_{\text{proj}} > 10000$ au, while in the inner region of $d_{\text{proj}} < 500$ au, the increase in polarization degree is caused mainly by the MRAT mechanism.

found the disruption of large grains of $a < 0.25 \mu\text{m}$ into smaller species as nanoparticles (i.e., $a < 100 \text{ \AA}$), which later on induces spinning dust emission at microwave frequencies below 100 GHz. [Truong et al. \(2022\)](#) studied the impacts of RAT-D in the Betelgeuse envelope and found their effects on the extinction and reddening of circumstellar dust at optical/near-IR wavelengths. The RAT-D effects depend on the grain internal structures and the local conditions of radiation fields and gas density and could be used for interpreting photometric and spectroscopic observations of evolved stars in the near-UV to near-IR regimes.

In Section 4.4 and 4.5, we show the impacts of the RAT-D mechanism on the thermal dust polarization in AGB envelopes and the polarization spectrum at far-IR/sub-mm wavelengths. In general, a dominant amount of smaller grains of $a < 0.5 \mu\text{m}$ by RAT-D (Figure 6) results in the reduction of the polarization degree, as shown in the Ideal model (the upper left panel of Figure 15 and the first row of Figure 18). The impact of rotational disruption is more efficient for porous grains with low S_{max} than for compact grains with high S_{max} , leading to the decrease in polarization degree with decreasing values of S_{max} . Yet, the decreasing level is slightly small because of the efficient external alignment of smaller grains with $a_{\text{align}} \sim a_{\text{min}} = 5 \text{ nm}$ (Figure 3), in comparison with the significant reduction of polarization degree by RAT-D found in the environments of the diffuse ISM and dense MCs ([Lee et al. 2020](#)).

In addition, in the analysis of $p - I/I_{\max}$ in Section 4.4 and the polarization spectrum in Section 4.5, we find the joint contribution of RAT-D and MRAT mechanism induces the inverse effect with the increase in polarization degree for porous grains with lower S_{max} .

This phenomenon occurs for PM grains undergoing MRAT alignment in the inner region of $r < 500$ au (the upper right panel of Figure 15), producing the flipping in the polarization spectrum for grains with lower S_{max} (the second row of Figure 18). The extension of the MRAT mechanism for SPM grains with iron inclusions (Figure 5) causes this effect potentially happen in the outer envelope of $r > 10000$ au. Consequently, by measuring thermal dust polarization from aligned grains, we can retrieve further information on dust properties in terms of both grain internal structures and magnetic properties of circumstellar grains.

5.4 Effects of magnetic field morphology on synthetic dust polarization

So far, we have stressed the importance of grain alignment and disruption in calculating the polarization of thermal dust emission in evolved star envelopes. Yet, even the conditions of the global magnetic fields themselves (i.e., magnetic field strength and geometry) significantly impact the measurement of dust polarization in the observed plane of the sky. The variation of the angle ψ between the local magnetic fields and the anisotropic radiation fields could impact the grain alignment efficiency by RATs ([Lazarian & Hoang 2007](#); [Hoang & Lazarian 2009](#); [Andersson et al. 2011](#); [Lazarian & Hoang 2021](#)), while the strength of magnetic fields could affect the magnetic relaxation of PM and SPM grains, which then affect the efficiency of MRAT alignment ([Hoang & Lazarian 2016](#); [Hoang et al. 2022](#)). More importantly, the orientation of the inclined magnetic fields with respect to the plane-of-sky strongly impacts the dust polarization de-

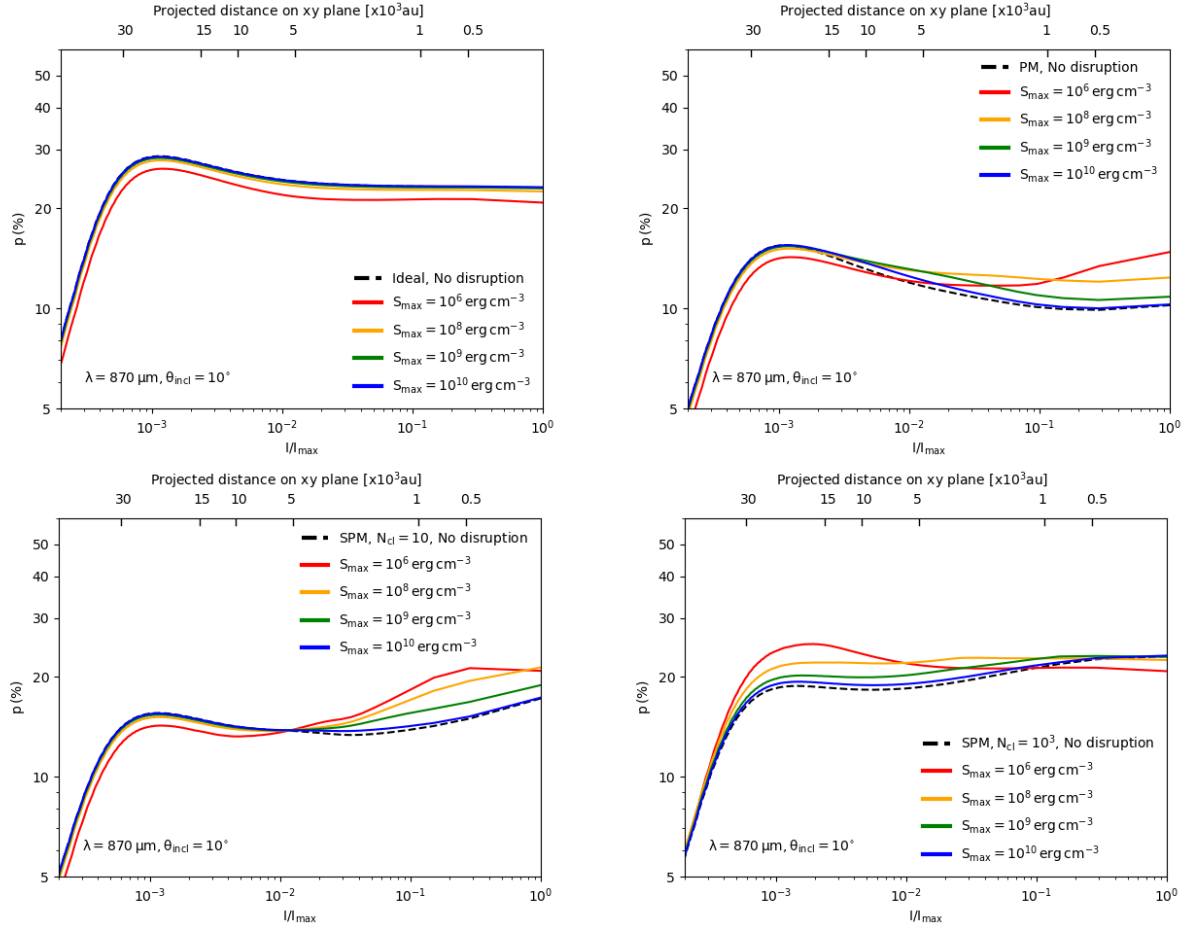


Figure 15. The effects of RAT-D on the intensity-dependent polarization degree observed in the face-on view (i.e., $\theta_{\text{incl}} = 10^\circ$) for grains with various values of S_{max} (solid color lines). The model for non-disrupted grains is added for comparison (dashed black line). In the Ideal model (upper left panel), the polarization is reduced for small porous grains (i.e., lower S_{max}) produced by RAT-D. By contrast, for PM grains (upper right panel), the polarization increases with decreasing S_{max} in the inner envelope of $d_{\text{proj}} < 500$ au due to the joint effects of RAT-D and MRAT. This pattern extends to the outer envelope of $d_{\text{proj}} > 10000$ au produced by SPM grains (lower panels) with the effective MRAT alignment.

gree by the projection effect (Reissl et al. 2017; Chen et al. 2019; Hu & Lazarian 2023), which has been studied in explaining the dust polarization observations in MCs and young stellar objects (YSOs) (Yang et al. 2016; Harrison et al. 2019; Tahani 2022).

In the context of evolved star envelopes with the dipole magnetic field, we show the magnetic field geometry affects the efficiency of the external alignment by RATs in Section 4.2.1. The difference in the angle ψ between the local fields and the radial stellar radiation at the equator region (i.e., $\psi \sim 0^\circ$) and the polar region (i.e., $\psi \sim 90^\circ$) causes the difference in the distribution of a_{align} (Figure 3), with smaller grains of $a_{\text{align}} \sim 5 - 10$ nm being aligned by RATs in the polar region of $r > 1000$ au, while the alignment size is larger at the equator of $a_{\text{align}} \sim 0.05 \mu\text{m}$. Moreover, the strong field strength toward the inner region of $r < 500$ au is a main factor in enhancing external alignment by MRAT for both PM and SPM grains (Figure 5), resulting in the increase in polarization degree as we mentioned earlier in Section 5.2.

The projection effect of the local magnetic field with the plane-of-sky is considerable in the calculation of the intensity-dependent polarization degree. In Section 4.3 and 4.4, by taking the calculations at different inclination angles, we find the change in the curvature of the three-dimensional dipole field could lead to the variation of the inclined magnetic field with the plane-of-sky and, therefore, enhance

or reduce the polarization degree at each radial envelope distance. The impact of inclined magnetic fields could subsequently explain the increase in p with decreasing envelope distance when observed in the face-on view of $\theta_{\text{incl}} = 10^\circ$ (Figure 12) and the decrease in p when observed in the edge-on view of $\theta_{\text{incl}} = 90^\circ$ (Figure 13).

The effects of magnetic field geometry are also presented in the calculation of the thermal dust polarization spectrum at far-IR/sub-mm. In Section 4.5, we show that the difference in the size distribution of aligned grains at the equator and the polar region due to magnetic field morphology (the upper panels of Figure 3) results in the difference in the spectrum of polarized thermal dust emission induced by grains in these regions. And as shown in Figure 16, the spectrum calculated in the face-on view is mostly produced by large aligned sizes in the equator region with the increasing polarization degree in longer wavelengths of $\lambda > 50 \mu\text{m}$. Meanwhile, in the calculation in the edge-on view (Figure 17), the spectrum is affected by the thermal dust emission from small aligned grains in the polar region, consequently causing the rise in the polarization degree toward shorter wavelengths of $\lambda < 50 \mu\text{m}$.

However, as discussed by Vlemmings (2019), the possibility of stellar magnetic fields having a toroidal configuration cannot be ruled out, which was detected in the envelopes of AGB stars, post-AGB objects, and PNe via maser polarization (Vlemmings et al. 2006;

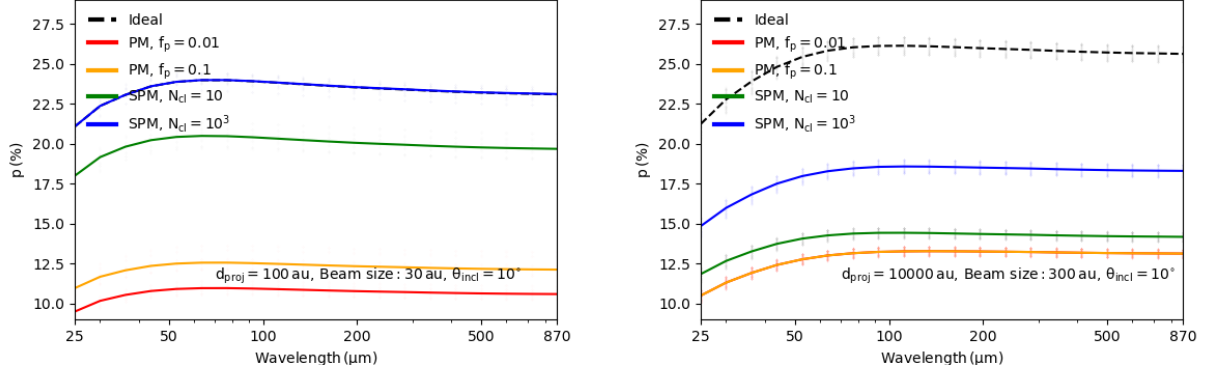


Figure 16. The face-on polarization spectrum at the wavelength from $25 \mu\text{m}$ to $870 \mu\text{m}$ induced by circumstellar dust at $d_{\text{proj}} = 100 \text{ au}$ (left panel) and $d_{\text{proj}} = 10000 \text{ au}$ (right panel) with different magnetic properties. The spectrum is produced mainly by large aligned grains at the equator, and the degree of polarization increases at the longer wavelengths $\lambda > 50 \mu\text{m}$.

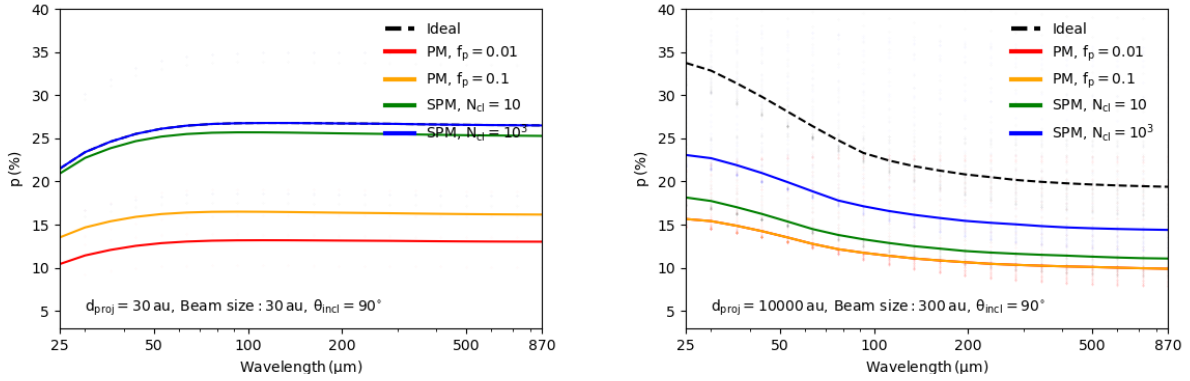


Figure 17. Same as Figure 16 but considering the edge-on observations at $d_{\text{proj}} = 30 \text{ au}$ (left panel) and $d_{\text{proj}} = 10000 \text{ au}$ (right panel). At the outer region of the AGB envelope $d_{\text{proj}} > 10000 \text{ au}$, the pattern of the polarization spectrum changes to the increase in p at the shorter wavelengths $\lambda < 50 \mu\text{m}$ due to the alignment of small grains in the polar region.

Leal-Ferreira et al. 2013) and dust continuum polarization (Greaves 2002; Sabin et al. 2015; Sabin et al. 2020). We adopt the three-dimensional structure of the toroidal fields as illustrated in the upper panels of Figure 19 in the xy -plane (left panel) and the xz -plane (right panels) and examine its effects on the measurement of dust polarization by using the updated POLARIS. The field strength varies with $B \propto r^{-1}$ as plotted in a dashed black line in the lower panel of Figure 19 followed by the radial profile of toroidal field strength from maser observations (Vlemmings 2019). In comparison with the dipole field (solid black line), the strength is reduced by a factor of 10 in the inner region of $r < 100 \text{ au}$, while it increases up to 1 mG in the outer envelope of $r \sim 10000 \text{ au}$.

The upper panels of Figure 20 show the maps of the minimum size of the external alignment by RATs a_{align} in both the xy - (left panel) and the xz -plane (right panel) under the impact of toroidal fields. The local magnetic fields are mostly perpendicular to the radiation fields (i.e., $\psi \sim 90^\circ$), which reduces the alignment efficiency and results in $a_{\text{align}} \sim 0.05 \mu\text{m}$ (dashed black line, see the lower panel of Figure 20).

The variation of the toroidal field strength significantly impacts the external alignment by MRAT, as can be seen in the profiles of $a_{\text{max,JB}}^{\text{DG}-0.5}$ and $a_{\text{max,JB}}^{\text{DG}-1}$ in the lower panel of Figure 20 by color lines. The reduction of the magnetic field strength in the inner region of $r < 100 \text{ au}$ leads to the considerably reduced effect of magnetic re-

laxation. Subsequently, the magnetic relaxation is strongly affected by the strong thermal fluctuation of electrons inside grains with increasing dust temperature $T_d > 100 \text{ K}$ (see Figure 2), causing the loss of external alignment by MRAT for PM grains in the inner envelope $r < 1000 \text{ au}$ (red and yellow lines). This results in the ‘polarization hole’ effect with a decrease in the polarization degree induced by PM grains to $\sim 5\% - 10\%$, as illustrated in the polarization map in Figure 21 and the profile of the mean $p - I/I_{\text{max}}$ in Figure 22. Meanwhile, in the outer envelope $r > 10000 \text{ au}$, the MRAT alignment efficiency increases significantly due to the combined effects of the increased toroidal field strength (Figure 19) and the reduced gas randomization (the lower panel of Figure 1). For SPM grains with iron inclusions (green and blue lines), they can be effectively aligned at high-J attractors in the inner region of $r < 1000 \text{ au}$. And the polarization produced by SPM grains is significantly enhanced up to $\sim 20\% - 40\%$, as shown in both Figure 21 and 22.

The geometry of the toroidal field itself concurrently affects the resulting polarization degree. The analysis of $p - I/I_{\text{max}}$ in Figure 22 shows that, under the projection effect of inclined magnetic fields lying to the plane-of-sky, the polarization degree tends to have a uniform value of $\sim 40\%$ when being calculated at $\theta_{\text{incl}} = 10^\circ$ (upper panels). Meanwhile, in the edge-on view at $\theta_{\text{incl}} = 90^\circ$ (lower panels), the change in the curvature of the toroidal field lines toward the outer region of $r > 10000 \text{ au}$ causes the decrease in polarization degree to

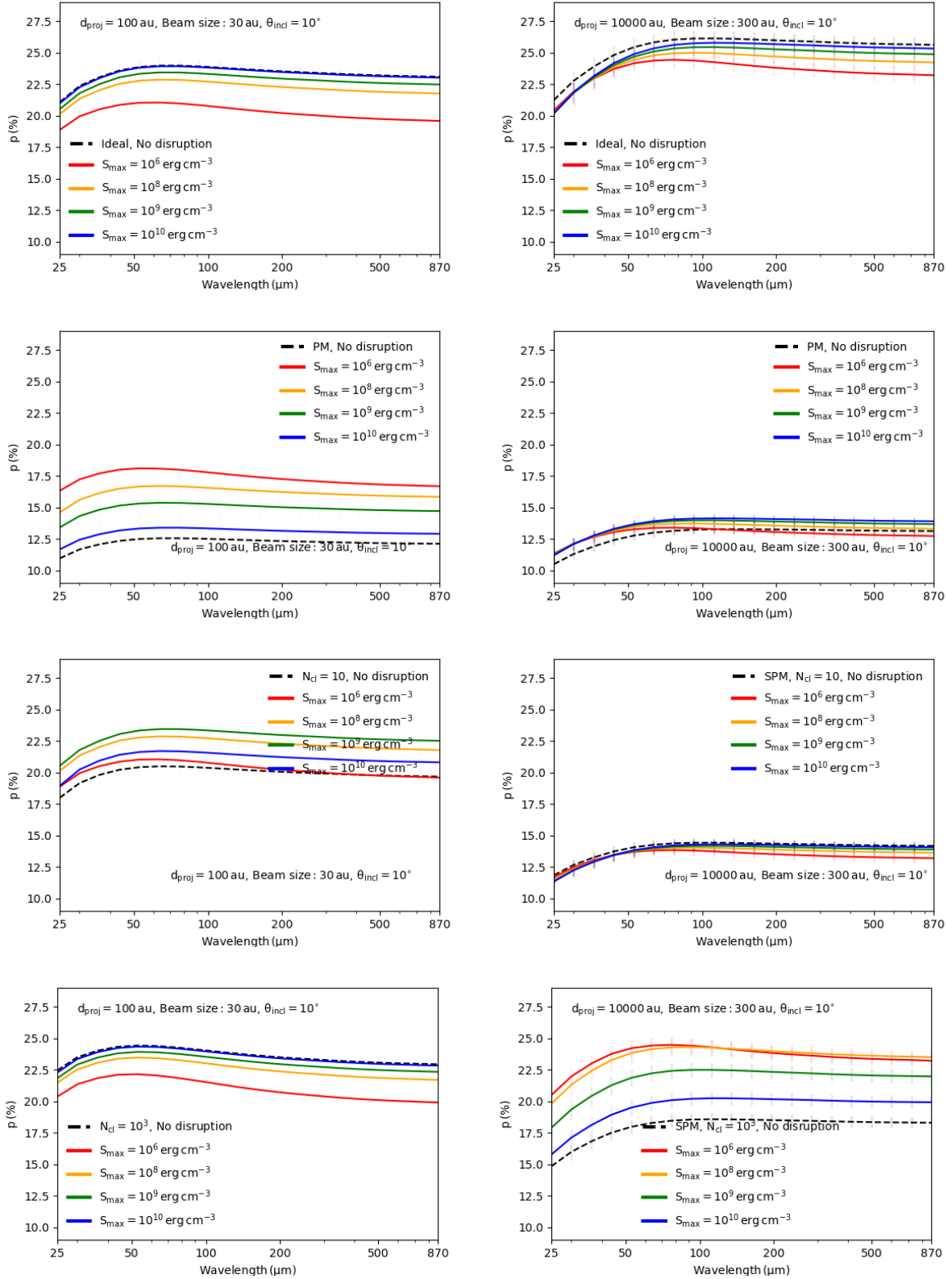


Figure 18. The impacts of RAT-D on the far-IR/sub-mm polarization spectrum at $d_{\text{proj}} = 100$ au (left panels) and $d_{\text{proj}} = 10000$ au (right panels) for various values of S_{max} (solid color lines) in comparison with the non-disrupted case (dashed black line), considering the face-on observation with $\theta_{\text{incl}} = 10^\circ$. The level of polarization degree decreases with decreasing S_{max} in the Ideal model (first row). The combined contribution of RAT-D and MRAT for PM grains (second row) results in the flipping in the polarized spectrum with the higher polarization degree for grains with lower S_{max} at $d_{\text{proj}} = 100$ au, and this feature shifts to $d_{\text{proj}} = 10000$ au for SPM grains (third and last row).

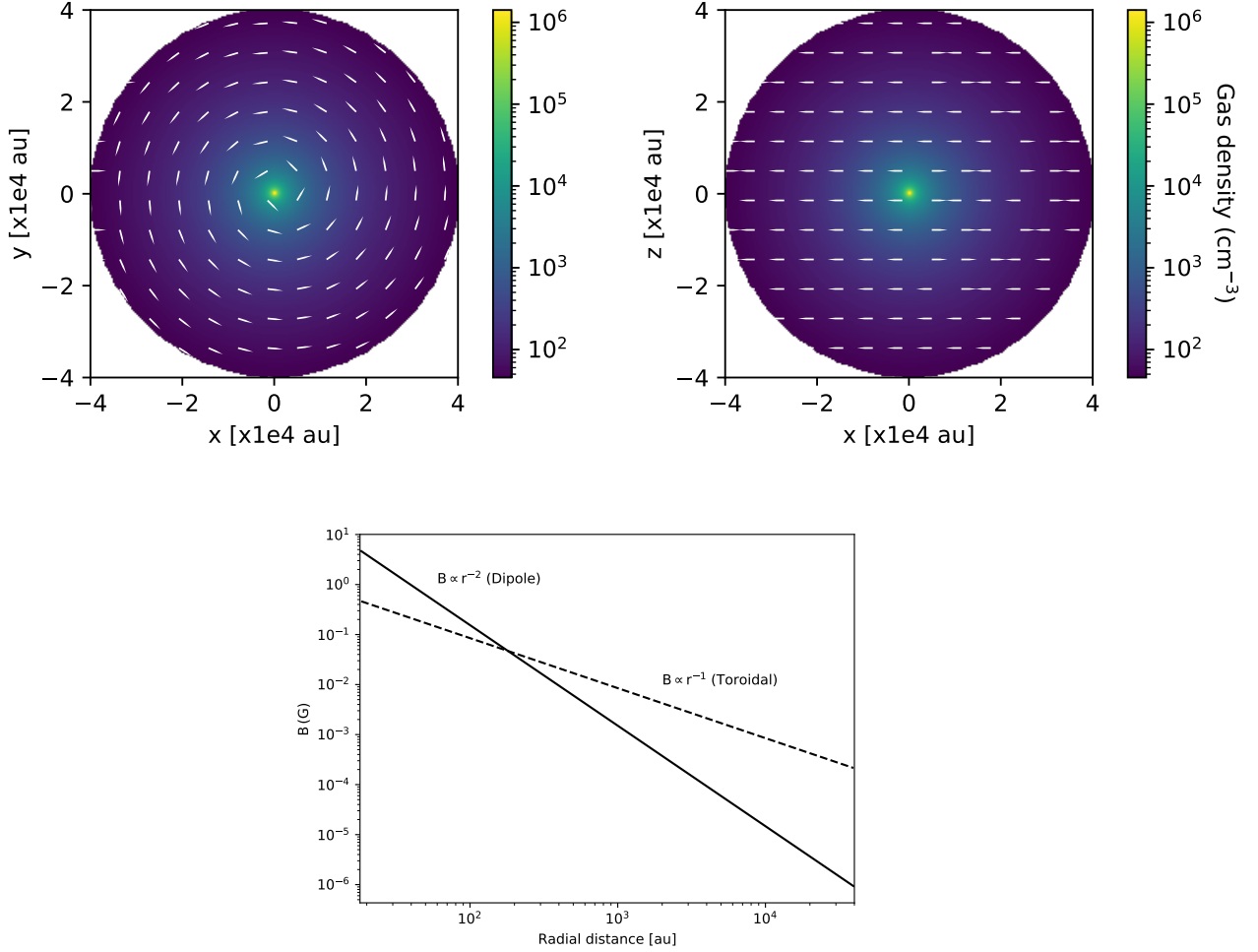


Figure 19. The morphology of the toroidal stellar magnetic field in the xy - (upper left panel) and xz - planes (upper right panel). The lower panel illustrates the strength of the toroidal field with respect to the envelope distance with $B \sim r^{-1}$ (solid black line), compared with the field strength of the dipole field (dashed black line).

$\sim 10\%$ at $d_{\text{proj}} \sim 30000$ au, as can be observed in the polarization maps (Figure 21). Hence, the impacts of magnetic field geometry on both grain alignment properties and the calculated polarization degree should be considered in the study of dust polarization from aligned grains in AGB envelopes.

5.5 Implications for constraining the global stellar magnetic fields

In Section 5.1, we discuss the internal relaxation by the Barnett effect is efficient, applying to both PM silicate grains at high- J attractors enhanced by magnetic relaxation in the inner envelope of $r < 500$ au (Figure 5) and grains at low- J in the outer envelope of $r > 10000$ au (Figure 4). This produces an abundance of grains having fast internal relaxation (then right internal alignment with $\mathbf{J} \parallel \mathbf{a}_1$). Additionally, silicate grains can have perfect external alignment by both RATs and MRAT with $\mathbf{J} \parallel \mathbf{B}$ (see Section 5.2). In consequence, this generates the polarized thermal dust emission with the shortest axes parallel to the magnetic fields ($\mathbf{P} \perp \mathbf{B}$), which could reproduce the large-scale magnetic field morphology through the polarization pattern, as illustrated in the envelope with the dipole field (Figure 8 and 9) and the toroidal field (Figure 21). Then, we can directly map the global

magnetic field derived from the polarimetric observations of far-IR/sub-mm instruments such as SOFIA/HAWC+, JCMT, CARMA, and ALMA. Combining with other measurements in the local B-fields from maser (Boboltz & Diamond 2005; Leal-Ferreira et al. 2013) and non-maser line emissions (Vlemmings et al. 2012; Huang et al. 2020), we can obtain a more general picture of the magnetic field geometry, which is a major step to understand further its role in the mass-loss mechanism in evolved star envelopes.

Furthermore, we have examined the dependence of the polarization degree on the magnetic geometry, particularly the projection effect on the plane-of-sky when calculated at different viewing inclination angles (Section 5.4). This effect mainly happens in the observation at the outer envelope of $r > 10000$ au where the variation of magnetic field curvature is significant, resulting in the modification of the polarization degree along the envelope distance as shown in the profile of $p - I/I_{\text{max}}$ (see Figure 14 for the dipole field and Figure 22 for the toroidal field). Therefore, by interpreting the intensity-dependent polarization degree from observational data, we could roughly estimate the observed inclination angle with respect to the line-of-sight, leading to the ultimate goal of reconstructing the three-dimensional global magnetic field presented in AGB envelopes.

In addition, the observed inclination angle can be determined

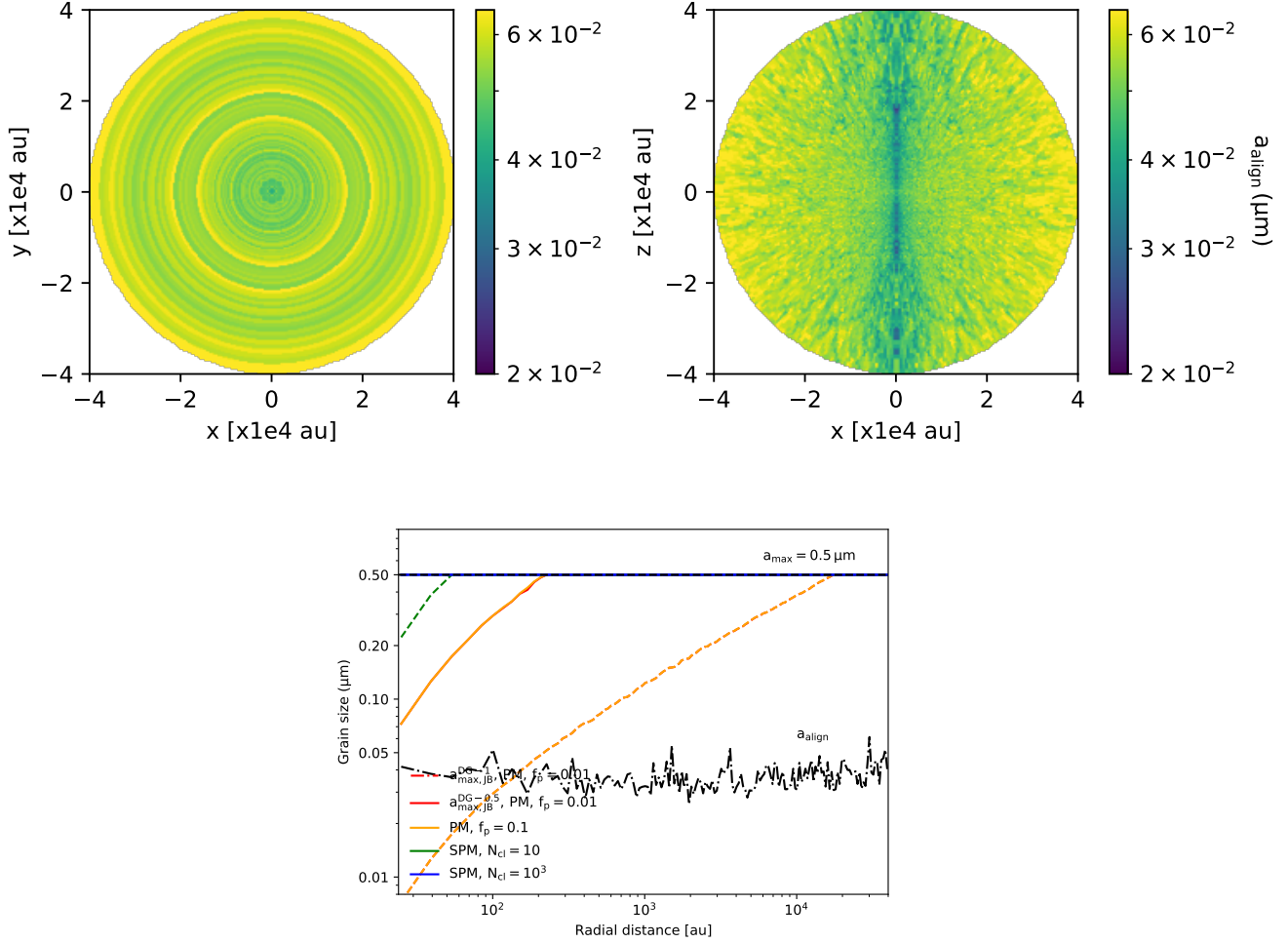


Figure 20. Upper panels: The distribution of aligned size a_{align} in xy - and xz - planes affected by the morphology of the toroidal field. The RAT alignment efficiency is reduced with large $a_{\text{align}} \sim 0.05 \mu\text{m}$ due to the dominance of the B-field components perpendicular to the radiation fields. Lower panel: The variation of the aligned size induced by RATs (a_{align} , dashed black line) and the critical sizes having efficient alignment by MRAT ($a_{\text{max,JB}}^{\text{DG}-0.5}$ and $a_{\text{max,JB}}^{\text{DG}-1}$, color lines) with the increasing envelope distance. The lower strength of the toroidal field strongly reduces the impact of magnetic relaxation. As a result, the MRAT alignment is reduced in the inner envelope of $r < 1000$ au with higher dust temperature.

through the thermal polarization spectrum at far-IR/sub-mm. In the case of the dipole field, the wavelength-dependent polarization degree induced by circumstellar dust is distinguishable between the observations at the face-on and edge-on views within the wavelengths of $\lambda \sim 25 - 100 \mu\text{m}$, especially at the outer envelope of $d_{\text{proj}} \sim 10000$ au as a result of the impact of magnetic field geometry on the alignment properties (Section 5.4). Thus, the resulting spectrum of polarized thermal emission from aligned grains could contribute to identifying the three-dimensional structure of the stellar magnetic field, which requires the future development of far-IR instruments with high spectral resolution in the next decades.

Note that the technique of tracing stellar magnetic fields via thermal dust polarization is highly applicable in the envelopes of O-rich AGB stars. In the C-rich AGB stars, [Hoang et al. \(2023\)](#) studied in detail the alignment of carbonaceous grains and found that the diamagnetic carbonaceous grains could have efficient internal alignment by inelastic relaxation and tend to be aligned with radiation field direction rather than magnetic field direction. Observations of thermal dust polarization from IRC+10216 by [Andersson et al. \(2022\)](#) reveal the radial polarization pattern, which is suggested as evidence

of carbonaceous alignment along the radiation direction with wrong internal alignment due to grain-gas drift flows. In future research, we will incorporate the alignment physics for carbonaceous grains developed by [Hoang et al. \(2023\)](#) into the updated POLARIS and perform modeling of dust polarization by carbonaceous grains.

5.6 Implications for constraining iron abundance incorporated into dust in AGB envelopes

It is believed that 90 % of iron is being locked inside the cosmic dust in the ISM environment, and they are initially formed in the ejecta of supernovae (SNe) and the outflows of evolved stars (e.g., [Jones 1990](#); [Tielens et al. 2005](#); [Dwek 2016](#)). The studies of gaseous depletion in the AGB envelopes showed that most iron is first condensed in a solid phase and presented in the dust formation zone at two to three stellar radii, which becomes one of the key ingredients of circumstellar dust in AGB outflows ([McDonald et al. 2011](#); [Dwek 2016](#); [Marini et al. 2019](#)). The theoretical modeling by [Karovicova et al. \(2013\)](#) and [Höfner et al. \(2022\)](#) showed the contribution of iron in olivine grains or in metallic form in the wind-driving mechanism and

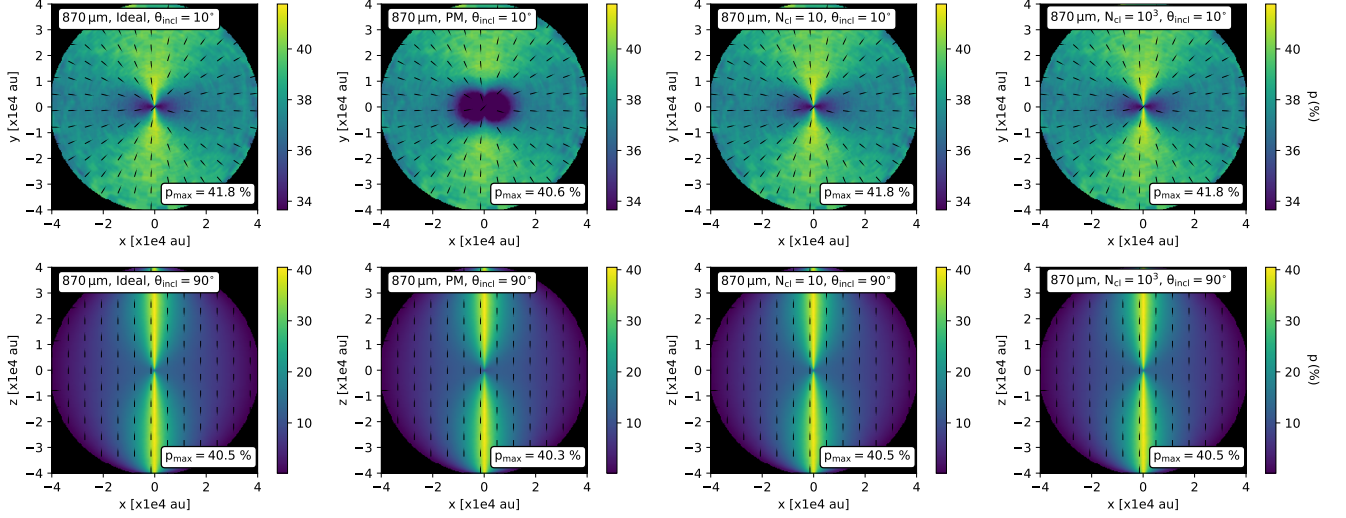


Figure 21. Polarization maps at $870\ \mu\text{m}$ produced by circumstellar dust with different magnetic properties on the large-scale of the envelope in the face-on (upper panels) and edge-on views (lower panels), indicating the toroidal field geometry through the polarization pattern with $\mathbf{P} \perp \mathbf{B}$. The loss of MRAT alignment toward the inner envelope (see Figure 20) produces the ‘polarization hole’ observed in the case of PM grains. The polarization degree is enhanced if grains contain high levels of iron inclusions, as shown in the case of SPM grains.

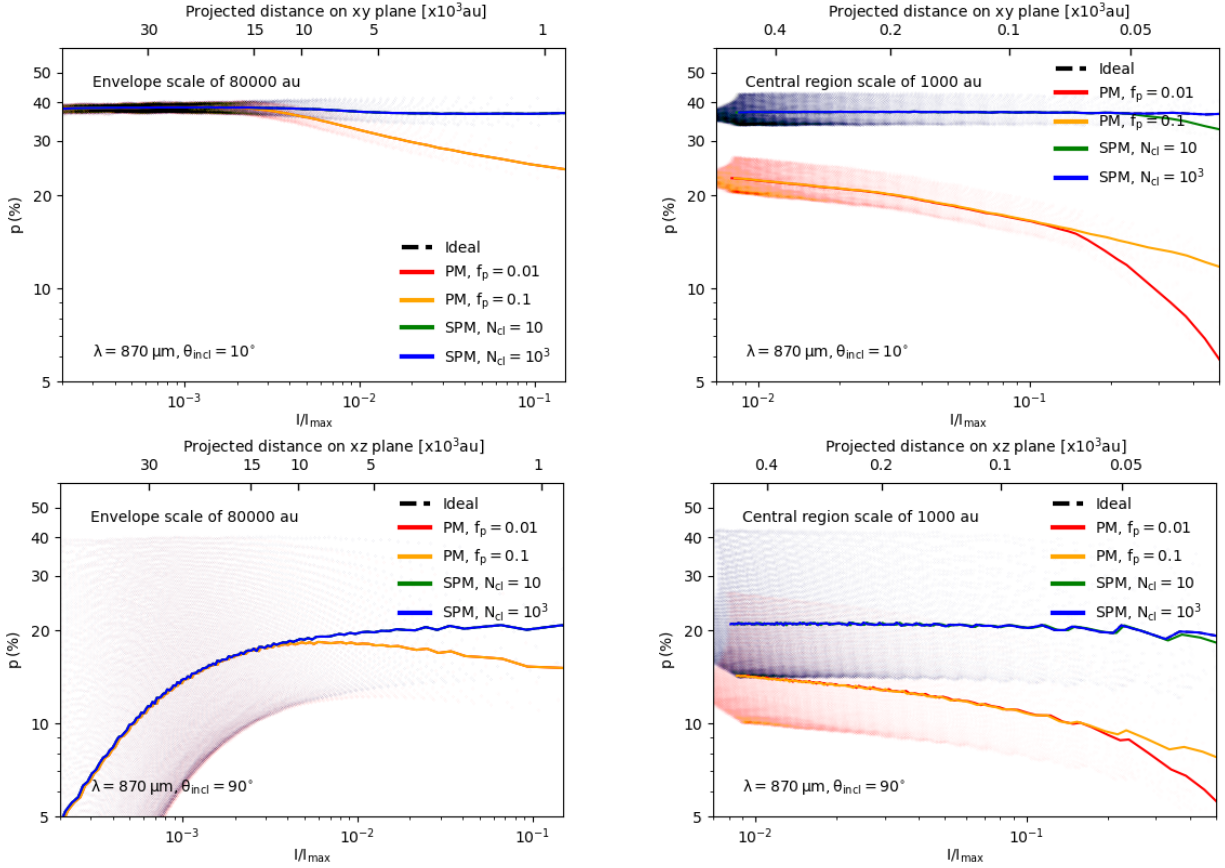


Figure 22. The mean polarization fraction p (%) with respect to the normalized intensity I/I_{max} calculating for the case of the toroidal stellar magnetic field. The polarization degree is considerably affected by the projection of the toroidal field in the plane-of-sky, resulting in the uniform polarization degree when observed in the face-on view (upper panels) and the reduced polarization fraction in the outer envelope of $d_{\text{proj}} > 10000\ \text{au}$ when observed in the edge-on view (lower panels). The polarization degree produced by PM grains decreases significantly in the inner region of $r < 1000\ \text{au}$ because of the reduction of RAT alignment. A higher abundance of iron inclusions in SPM grains can enhance the level of polarization degree.

could potentially be detected in the signature of mid-IR interferometric spectroscopy. Yet, determining iron levels inside grains has been challenging in astronomical observations. [Hoang & Lazarian \(2016\)](#) studied the alignment for grains with magnetic inclusions and showed the possibility of constraining the level of iron inclusions in cosmic dust via sub-mm polarization, which was successfully used for interpreting ALMA polarimetric observations in dense environments as protostellar cores/disks ([Giang et al. 2023](#)) and protoplanetary disks ([Lazarian & Hoang 2019](#)).

In Section 5.2, we mention the crucial role of embedded iron in enhancing the polarization degree produced by PM and SPM grains in AGB envelopes as a result of the enhanced efficiency of internal and external alignment with B-fields (Section 5.1). The effects of embedded iron for different magnetic properties of grains are more prominent in the inner envelope of $r < 500$ au in which the alignment is mainly impacted by the efficiency of the MRAT mechanism, as illustrated in the results of $p - I/I_{\max}$ regardless of the configuration of magnetic field geometry (see Figure 14 and 22). By measuring the dependency of polarization degree induced by circumstellar dust on the intensity at sub-mm bands, we could first identify the configuration of iron distributed inside grains (i.e., PM or SPM grains) and, later on, determine the levels of embedded iron through the level of polarization degree. This provides proper insight into circumstellar dust properties and could support expanding our fundamental knowledge of their formation and evolution within the evolved star outflows.

5.7 Comparison to far-IR/sub-mm dust polarization observations with SOFIA/HAWC+

In this section, we compare our numerical results of dust polarization with observations at far-IR/sub-mm wavelengths, taking the polarimetric observation of the IK Tau envelope by SOFIA/HAWC+ as an example ([Andersson et al.](#), in preparation). We take the Level 4 product of the archival data of IK Tau captured by Band A of the HAWC+ instrument at $53 \mu\text{m}$ with the beam size of 4.84 arcsecond². This corresponds to the physical resolution of ~ 1282.6 au at the stellar distance of 265 pc (see Table 1). We take the cuts of $p < 50\%$, $p/\sigma_p < 3$, and $I/\sigma_I < 200$ ([Gordon et al. 2018](#)) to ensure the quality of the polarimetric data for further analysis.

The left panel of Figure 23 shows the polarization map of the IK Tau envelope when zooming toward the central source. As rotating the polarization vectors to 90 degrees, the data could reproduce the dipole structure of stellar magnetic fields, as same as the polarization pattern in the edge-on view presented in our modeling (see Figure 8 and 9).

To explore the properties of dust and magnetic fields through dust polarization, we analyze the dependence of polarization fraction p (%) on the intensity I measured at each projected distance toward the central star, as shown in the right panel of Figure 23. The observed mean dust polarization degree (solid black line) is significantly low in the outer region of $r \sim 2600$ au with $p \sim 3\%$, and decreases to $\sim 1\%$ at $r \sim 500$ au. The decrease in the observed polarization fraction is quite close to that for the modeled $p - I$ produced by PM grains in edge-on observations (dashed color lines) for various inclination angles $\theta_{\text{incl}} = 60^\circ - 90^\circ$. It is caused by both the effect of PM grains at low-J attractors having low internal relaxation (Section 5.1) and the impact of dipole magnetic fields on the measured polarization in the plane-of-sky (Section 5.4). Consequently, circumstellar grains

are likely to be paramagnetic, in which iron atoms are diffusely distributed rather than in the form of iron clusters within silicate grains.

Additionally, compared to our modeling results (dashed color lines), the mean polarization fraction observed by SOFIA/HAWC+ (solid black line) is lower by a factor of 7 (solid color lines). This reveals that circumstellar grains might have a less elongated shape rather than a highly elongated shape of axial ratio $s = 0.5$ adopted for our modeling. Indeed, as shown in [Draine & Fraisse \(2009\)](#) and [Draine & Hensley \(2021\)](#), the polarization fraction could be decreased by a factor of 1.5 - 2 when the axial ratio increases from $s = 0.5$ (more elongated) to $s = 0.71$ (less elongated). The not highly elongated shape of circumstellar grains seems reasonable because they are newly formed by the condensation of gaseous molecules and do not undergo significant processing by grain-grain collisions ([Verhoelst et al. 2009](#); [Gobrecht et al. 2016](#)). Our findings highlight the importance of polarimetric observations from far-IR/sub-mm instruments in understanding magnetic field and dust properties within AGB outflows.

There are other possibilities that cause the difference between the modeled and observational data. One possible factor is that the stellar magnetic field strength of IK Tau may not be as high as we adopted from the measurement by maser polarization (the lower panel of Figure 1), in which the magnetic field strength may be resolved in small samples of the envelope ([Soker 2002](#); [Vlemmings 2019](#)). The strength of stellar B-fields may be lower in the entire envelope and could result in a lower polarization degree as shown in the SOFIA/HAWC+ observation of IK Tau (right panel of Figure 23). Another possibility is the presence of magnetohydrodynamic (MHD) turbulence in stellar magnetic fields could reduce the degree of polarization in the plane-of-sky, similar to what happened in the observations of MCs and the diffuse ISM (see [Planck Collaboration et al. 2020](#)). The role of MHD turbulence in driving stellar winds was theoretically studied by [Pascoli \(2020\)](#); however, it requires high spatial resolution observations for probing their existence in the global stellar magnetic fields in AGB envelopes. These possibilities could contribute to improving our interpretation of the currently available observational data.

5.8 Dependence of thermal dust polarization from aligned grains on the properties of AGB envelopes

Throughout this research, we adopt the numerical modeling of thermal dust polarization from aligned grains for a specific case of the IK Tau envelope and emphasize its significant roles in mapping stellar magnetic fields (Section 5.5) and constraining the abundance of iron locked inside grains (Section 5.6). The modeling can also be applied in the envelopes of other O-rich AGB and RSG stars with strong stellar magnetic fields of several mG-G (see [Vlemmings 2019](#)) and thus, motivate further studies of magnetic fields and dust in evolved star envelopes through far-IR/sub-mm polarization observations.

Nevertheless, the properties of evolved stars, particularly the stellar mass-loss rate and its luminosity, could directly affect the alignment of circumstellar grains and the results of thermal dust polarization. [Reimers \(1975, 1977\)](#) first described the relation between the evolved star mass-loss rate and other stellar parameters as $\dot{M} \propto L_* R_* / M_*$ from a sample of photometric and spectroscopic observations of red giants, supergiants and AGB stars. Various studies described the empirical formulation of the stellar mass-loss rate based on observations and numerical modeling (e.g., [de Jager et al. 1988](#); [Vassiliadis & Wood 1993](#); [van Loon et al. 2005](#); [Schröder & Cuntz 2005](#); [Danilovich et al. 2015](#); [Prager et al. 2022](#)), mostly agreed with the positive correlation between the mass-loss rate and the stellar lumi-

² <https://irsa.ipac.caltech.edu/Missions/sofia.html>

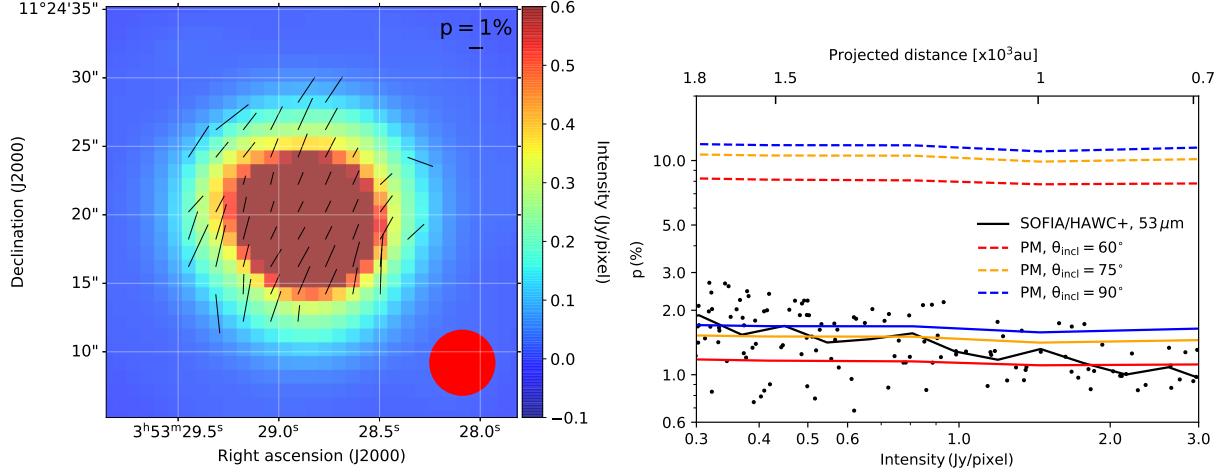


Figure 23. Left panel: The polarization map overlotted on the intensity for the central region of the IK Tau envelope observed at Band A of SOFIA/HAWC+ at the wavelength of $53 \mu\text{m}$ (Andersson et al., in preparation) with the beam size of 4.84 arcsecond (red circle). The polarization fraction is represented by the length of polarization vectors. Right panel: Comparison of the polarization fraction from our numerical modeling with POLARIS for PM grains with $f_p = 0.1$ in edge-on observations $\theta_{\text{incl}} = 60^\circ - 90^\circ$ (dashed color lines) to the observational data (black data points). The solid color lines show our modeling results multiplied by a factor of $1/7$, which can agree better with the data (see Section 5.7 for discussion).

nosity. The increased stellar luminosity produces stronger RATs onto dust grains (Equation 3), while the increased mass-loss rate leads to the increased gas density (Equation 1) and the enhancement of gas randomization. This could result in different scenarios of internal and external alignment of circumstellar grains within the evolved star outflows, and then, modify the calculation of thermal dust polarization. The effects of AGB mass-loss rates and their luminosities will be taken into consideration in the main numerical modeling to generalize the implications of thermal dust polarization from aligned grains in studying magnetic fields and dust properties in evolved star environments, which will be presented in our follow-up study.

6 SUMMARY

Our study concentrates on modeling the physics of grain alignment and rotational disruption by RATs for circumstellar grains in the envelope of IK Tau. Using the updated version of POLARIS developed by Giang et al. (2023), we then perform the numerical modeling of thermal dust polarization induced by aligned grains and infer the main applications in investigating magnetic fields and dust properties in evolved star outflows via far-IR/sub-mm polarimetry. The main findings are summarized as follows:

(i) Under the strong radiation field from the central AGB star, paramagnetic (PM) silicate grains at high-J attractors can achieve internal relaxation and external Larmor precession faster than the randomization by gas species and then are effectively aligned with the ambient B-fields. The efficiency of grain alignment is significantly increased by the magnetic relaxation induced by the strong magnetic field of $B \sim 10 \text{ mG} - 1 \text{ G}$, allowing grains to have efficient alignment in the dense inner envelope of $r < 500 \text{ au}$ with $n_{\text{gas}} > 10^6 \text{ erg cm}^{-3}$. Meanwhile, grains at low-J attractors can have perfect alignment in the less dense environment of the outer envelope of $r > 10000 \text{ au}$. The presence of iron inclusions incorporated into superparamagnetic (SPM) grains with increasing level can enhance grain alignment

efficiency and helps them to be aligned with stellar magnetic fields in the entire envelope.

(ii) Both PM and SPM silicate grains with efficient internal and external alignment with the shortest axis perpendicular to the B-fields in the AGB envelope can produce the polarized thermal dust emission with the pattern of $\mathbf{P} \perp \mathbf{B}$ at far-IR/sub-mm wavelengths. Hence, we can reproduce the global structure of the stellar magnetic field by rotating the polarization vectors to 90 degrees.

(iii) The polarization degree produced by PM grains could increase up to $\sim 10\%$ toward the central region of $r < 500 \text{ au}$ because of the enhanced grain alignment by MRAT due to the strong stellar magnetic field. The polarization degree is considerably higher for SPM grains up to $\sim 20 - 40\%$, and this feature could be extended to the outer envelope of $r > 10000 \text{ au}$ due to the increased MRAT alignment efficiency with increasing level of iron inclusions.

(iv) The rotational disruption by RATs (RAT-D) can constrain the upper size of silicate grains presented in AGB envelopes and modify the level of polarization degree. The increasing population of small grains of $a < 0.5 \mu\text{m}$ produced by RAT-D can induce the lower polarization degree. The impact of RAT-D is more prominent for porous grains with lower S_{max} and causes a decrease in the total polarization degree. Nevertheless, the enhancement of alignment efficiency by MRAT is a major contribution to the enhanced alignment of the high amount of porous grains rather than compact grains. The combined contribution of MRAT and RAT-D leads to the inverse effect with the increased polarization degree for porous grains.

(v) The stellar magnetic field strength and geometry can directly impact the properties of grain alignment and dust polarization due to the projection effect of magnetic fields with respect to the observed plane of the sky. The magnetic field morphology can cause the enhancement or reduction of the degree of polarization, depending strongly on the variation of the magnetic field along the line-of-sight when being observed at different inclination angles.

(vi) Thermal dust polarization from aligned grains is essential for determining the global magnetic field morphology in the evolved star envelopes. The main structure of the stellar magnetic field can be

mapped through the polarization pattern in the plane-of-sky, while the observed inclination angle can be identified through the $p - I$ relationship and the spectrum of polarized thermal dust emission. This provides a key tool for reconstructing the three-dimensional geometry of the magnetic field of AGB stars.

(vii) The characterization of thermal dust polarization from aligned grains can potentially help us constrain the level of iron inclusions locked inside circumstellar dust. This lays out the major step for understanding the underlying magnetic properties of circumstellar dust and the important role of iron in the formation and evolution of circumstellar dust in AGB envelopes.

(viii) We discuss the implications of our numerical modeling for interpreting far-IR observations of IK Tau envelopes by SOFIA/HAWC+ (Andersson et al., in preparation). The pattern of polarization vectors illustrates the dipole structure of the stellar magnetic field similar to what we obtain in our modeling in the edge-on view, while the low, decreased intensity-dependent polarization degree with $p \sim 1\% - 3\%$ implies circumstellar grains should be paramagnetic with the diffuse distribution of iron atoms. Moreover, the lower degree of observed polarization than our modeling suggests that dust grains in the IK Tau are less elongated than our chosen axial ratio $s = 0.5$.

(ix) The numerical modeling of thermal dust polarization from aligned grains can be applicable to other O-rich evolved star environments with strong magnetic field strengths up to mG-G (Vlemmings 2019). However, the modeling results of grain alignment and thermal dust polarization could be impacted by stellar parameters such as mass-loss rates and stellar luminosities for different AGB and RSG stars. Our follow-up study will consider the effects of stellar properties to further investigate dust properties and magnetic field morphology via thermal dust polarization in various conditions of evolved star envelopes.

Acknowledgement: T.H. acknowledges the support by the National Research Foundation of Korea (NRF) grant (2019R1A2C1087045) funded by the Korean government (MSIT). Dieu D. Nguyen is grateful to the LABEX Lyon Institute of Origins (ANR- 10-LABX-0066) Lyon for its financial support within the program “Investissements d’Avenir” of the French government operated by the National Research Agency (ANR). N.B.N. was funded by the Master, Ph.D. Scholarship Programme of Vingroup Innovation Foundation (VINIF), code VINIF.2022.TS083. We thank members of Vietnam Astrophysics Research NETWORK (VARNET) for the contribution in commenting and improving the quality of this paper.

REFERENCES

- Adam C., Ohnaka K., 2019, *A&A*, **628**, A132
- Airapetian V. S., Ofman L., Robinson R. D., Carpenter K., Davila J., 2000, *ApJ*, **528**, 965
- Airapetian V., Carpenter K. G., Ofman L., 2010, *ApJ*, **723**, 1210
- Andersson B. G., Pintado O., Potter S. B., Straižys V., Charcos-Llorens M., 2011, *A&A*, **534**, A19
- Andersson B. G., Lazarian A., Vaillancourt J. E., 2015, *ARA&A*, **53**, 501
- Andersson B. G., et al., 2022, *ApJ*, **931**, 80
- Barnett S. J., 1915, *Physical Review*, **6**, 239
- Bethell T. J., Chepurnov A., Lazarian A., Kim J., 2007, *ApJ*, **663**, 1055
- Boboltz D. A., Diamond P. J., 2005, *ApJ*, **625**, 978
- Cardelli J. A., Clayton G. C., Mathis J. S., 1989, *ApJ*, **345**, 245
- Chen C.-Y., King P. K., Li Z.-Y., Fissel L. M., Mazzei R. R., 2019, *MNRAS*, **485**, 3499
- Cox E. G., Harris R. J., Looney L. W., Li Z.-Y., Yang H., Tobin J. J., Stephens I., 2018, *ApJ*, **855**, 92
- Cranmer S. R., Saar S. H., 2011, *ApJ*, **741**, 54
- Crutcher R. M., 2012, *ARA&A*, **50**, 29
- Danilovich T., et al., 2015, *A&A*, **581**, A60
- Davis Leverett J., Greenstein J. L., 1951, *ApJ*, **114**, 206
- De Beck E., et al., 2019, *BAAS*, **51**, 374
- Decin L., et al., 2010, *A&A*, **516**, A69
- Decin L., Richards A. M. S., Danilovich T., Homan W., Nuth J. A., 2018, *A&A*, **615**, A28
- Dolginov A. Z., Mitrofanov I. G., 1976, *Ap&SS*, **43**, 291
- Draine B. T., 2011, *Physics of the Interstellar and Intergalactic Medium*. Princeton University Press
- Draine B. T., Fraisse A. A., 2009, *ApJ*, **696**, 1
- Draine B. T., Hensley B. S., 2021, *ApJ*, **909**, 94
- Draine B. T., Lee H. M., 1984, *ApJ*, **285**, 89
- Draine B. T., Salpeter E. E., 1979, *ApJ*, **231**, 77
- Draine B. T., Weingartner J. C., 1996, *ApJ*, **470**, 551
- Dwek E., 2016, *ApJ*, **825**, 136
- Ferrarotti A. S., Gail H. P., 2006, *A&A*, **447**, 553
- Fox M. W., Wood P. R., 1985, *ApJ*, **297**, 455
- García-Segura G., Langer N., Różyczka M., Franco J., 1999, *ApJ*, **517**, 767
- Giang N. C., Hoang T., 2021, *ApJ*, **922**, 47
- Giang N. C., Hoang T., Tram L. N., 2020, *ApJ*, **888**, 93
- Giang N. C., Hoang T., Tram L. N., Dieu N. D., Diep P. N., Phuong N. T., Tuan B. V., Truong B., 2022, *ApJ*, **936**, 108
- Giang N. C., Hoang T., Kim J.-G., Tram L. N., 2023, *MNRAS*, **520**, 3788
- Gobrecht D., Cherkneff I., Sarangi A., Plane J. M. C., Bromley S. T., 2016, *A&A*, **585**, A6
- Gordon M. S., et al., 2018, *arXiv e-prints*, p. arXiv:1811.03100
- Greaves J. S., 2002, *A&A*, **392**, L1
- Greenberg J., 1968, University of Chicago Press, 7, 221
- Hale D. D. S., et al., 1997, *ApJ*, **490**, 407
- Harrison R. E., et al., 2019, *ApJL*, **877**, L2
- Hensley B. S., Draine B. T., 2021, *ApJ*, **906**, 73
- Herranen J., Lazarian A., Hoang T., 2021, *ApJ*, **913**, 63
- Hildebrand R. H., 1988, Royal Astronomical Society, Quarterly Journal (ISSN 0035-8738), vol. 29, Sept. 1988, p. 327-351., 29, 327
- Hoang T., 2022, *ApJ*, **928**, 102
- Hoang T., Lazarian A., 2008, *MNRAS*, **388**, 117
- Hoang T., Lazarian A., 2009, *ApJ*, **697**, 1316
- Hoang T., Lazarian A., 2014, *MNRAS*, **438**, 680
- Hoang T., Lazarian A., 2016, *ApJ*, **831**, 159
- Hoang T. D. et al., 2022, *ApJ*, **929**, 27
- Hoang T., Tram L. N., Lee H., Ahn S.-H., 2019, *Nature Astronomy*, **3**, 766
- Hoang T., Giang N. C., Tram L. N., 2020, *ApJ*, **895**, 16
- Hoang T., Tram L. N., Lee H., Diep P. N., Ngoc N. B., 2021, *ApJ*, **908**, 218
- Hoang T., Tram L. N., Minh Phan V. H., Giang N. C., Phuong N. T., Dieu N. D., 2022, *AJ*, **164**, 248
- Hoang T., Phan V. H. M., Tram L. N., 2023, *arXiv e-prints*, p. arXiv:2301.07832
- Höfner S., 2008, *A&A*, **491**, L1
- Höfner S., Olofsson H., 2018, *A&ARv*, **26**, 1
- Höfner S., Bladh S., Aringer B., Ahuja R., 2016, *A&A*, **594**, A108
- Höfner S., Bladh S., Aringer B., Eriksson K., 2022, *A&A*, **657**, A109
- Hu Y., Lazarian A., 2023, *MNRAS*, **519**, 3736
- Huang K.-Y., Kembal A. J., Vlemmings W. H. T., Lai S.-P., Yang L., Agudo I., 2020, *ApJ*, **899**, 152
- Hull C. L., et al., 2014, *The Astrophysical Journal Supplement Series*, **213**, 13
- Jones A. P., 1990, *MNRAS*, **245**, 331
- Jones R. V., Spitzer Lyman J., 1967, *ApJ*, **147**, 943
- Karovicova L., Wittkowski M., Ohnaka K., Boboltz D. A., Fossat E., Scholz M., 2013, *A&A*, **560**, A75
- Khoury T., et al., 2016, *A&A*, **591**, A70
- Kim H., Wyrowski F., Menten K. M., Decin L., 2010, *A&A*, **516**, A68
- Kylafis N. D., 1983, *ApJ*, **267**, 137
- Lazarian A., Hoang T., 2007, *MNRAS*, **378**, 910
- Lazarian A., Hoang T., 2019, *ApJ*, **883**, 122
- Lazarian A., Hoang T., 2021, *ApJ*, **908**, 12

- Leal-Ferreira M. L., Vlemmings W. H. T., Kemball A., Amiri N., 2013, *A&A*, **554**, A134
- Lee H., Hoang T., Le N., Cho J., 2020, *ApJ*, **896**, 44
- Lucy L. B., 1999, *A&A*, **344**, 282
- Maercker M., Danilovich T., Olofsson H., De Beck E., Justtanont K., Lombaert R., Royer P., 2016, *A&A*, **591**, A44
- Marini E., Dell'Agli F., Di Criscienzo M., Puccetti S., García-Hernández D. A., Mattsson L., Ventura P., 2019, *ApJL*, **871**, L16
- Martin P. G., 1974, *ApJ*, **187**, 461
- Marvel K. B., 2005, *AJ*, **130**, 261
- Mathis J. S., Rumpl W., Nordsieck K. H., 1977, *ApJ*, **217**, 425
- McDonald I., Zijlstra A. A., Sloan G. C., Matsuura M., 2011, in Kerschbaum F., Lebzelter T., Wing R. F., eds, *Astronomical Society of the Pacific Conference Series Vol. 445, Why Galaxies Care about AGB Stars II: Shining Examples and Common Inhabitants*, p. 241
- Ngoc N. B., et al., 2021, *ApJ*, **908**, 10
- Ngoc N. B., et al., 2023, arXiv preprint arXiv:2302.10543
- Nordhaus J., Blackman E. G., Frank A., 2007, *MNRAS*, **376**, 599
- Pascoli G., 2020, *PASP*, **132**, 034203
- Planck Collaboration et al., 2020, *A&A*, **641**, A12
- Prager H. A., Willson L. A., Marengo M., Creech-Eakman M. J., 2022, *ApJ*, **941**, 44
- Purcell E. M., 1979, *ApJ*, **231**, 404
- Reimers D., 1975, in , *Problems in stellar atmospheres and envelopes.* Springer-Verlag New York, Inc., pp 229–256
- Reimers D., 1977, *A&A*, **61**, 217
- Reissl S., Wolf S., Brauer R., 2016, *A&A*, **593**, A87
- Reissl S., Seifried D., Wolf S., Banerjee R., Klessen R. S., 2017, *A&A*, **603**, A71
- Reissl S., Guillet V., Brauer R., Levrier F., Boulanger F., Klessen R. S., 2020, *A&A*, **640**, A118
- Reissl S., Stutz A. M., Klessen R. S., Seifried D., Walch S., 2021, *MNRAS*, **500**, 153
- Sabin L., Zijlstra A. A., Greaves J. S., 2007, *MNRAS*, **376**, 378
- Sabin L., Hull C. L. H., Plambeck R. L., Zijlstra A. A., Vázquez R., Navarro S. G., Guillén P. F., 2015, *MNRAS*, **449**, 2368
- Sabin L., et al., 2020, *MNRAS*, **495**, 4297
- Schröder K. P., Cuntz M., 2005, *ApJL*, **630**, L73
- Sciicluna P., Siebenmorgen R., Wesson R., Blommaert J. A. D. L., Kasper M., Voshchinnikov N. V., Wolf S., 2015, *A&A*, **584**, L10
- Sciicluna P., et al., 2020, arXiv e-prints, p. arXiv:2002.03100
- Seifried D., Walch S., Reissl S., Ibáñez-Mejía J. C., 2019, *MNRAS*, **482**, 2697
- Seifried D., Walch S., Weis M., Reissl S., Soler J. D., Klessen R. S., Joshi P. R., 2020, *MNRAS*, **497**, 4196
- Soker N., 2002, *MNRAS*, **336**, 826
- Tahani M., 2022, *Frontiers in Astronomy and Space Sciences*, **9**, 940027
- Thirumalai A., Heyl J. S., 2013, *MNRAS*, **430**, 1359
- Tielens A. G. G. M., Waters L. B. F. M., Bernatowicz T. J., 2005, in Krot A. N., Scott E. R. D., Reipurth B., eds, *Astronomical Society of the Pacific Conference Series Vol. 341, Chondrites and the Protoplanetary Disk*, p. 605
- Tram L. N., Hoang T., 2022, *Frontiers in Astronomy and Space Sciences*, **9**, 923927
- Tram L. N., Hoang T., Soam A., Lesaffre P., Reach W. T., 2020, *ApJ*, **893**, 138
- Tram L. N., Hoang T., Lee H., Santos F. P., Soam A., Lesaffre P., Gusdorf A., Reach W. T., 2021a, *ApJ*, **906**, 115
- Tram L. N., et al., 2021b, *ApJ*, **923**, 130
- Truong B., et al., 2022, *ApJ*, **936**, 101
- Vassiliadis E., Wood P. R., 1993, *ApJ*, **413**, 641
- Verhoelst T., van der Zypen N., Hony S., Decin L., Cami J., Eriksson K., 2009, *A&A*, **498**, 127
- Vlemmings W., 2019, *IAU Symposium*, **343**, 19
- Vlemmings W. H. T., Diamond P. J., Imai H., 2006, *Nature*, **440**, 58
- Vlemmings W. H. T., Ramstedt S., Rao R., Maercker M., 2012, *A&A*, **540**, L3
- Vlemmings W. H. T., et al., 2017, *A&A*, **603**, A92
- Wing R. F., Lockwood G. W., 1973, *ApJ*, **184**, 873
- Yang H., Li Z.-Y., Looney L., Stephens I., 2016, *MNRAS*, **456**, 2794
- de Jager C., Nieuwenhuijzen H., van der Hucht K. A., 1988, *A&AS*, **72**, 259
- van Loon J. T., Cioni M. R. L., Zijlstra A. A., Loup C., 2005, *A&A*, **438**, 273

This paper has been typeset from a $\text{\TeX}/\text{\LaTeX}$ file prepared by the author.